6th BSME International Conference on Thermal Engineering (ICTE 2014)

A computational fluid-structure interaction technique to observe the quenching characteristics of a steel part

Pratik Sarker*, Uttam K. Chakravarty

Department of Mechanical Engineering, University of New Orleans, New Orleans, Louisiana 70148, USA

Abstract

It is a common practice for steel parts to be subjected to industrial quenching processes for improving certain material properties. Machine components made of steel are widely used in heavily loaded mechanisms where they have to withstand high dynamic torsional, compressive, and repetitive reverse stresses. Subsequently, they need to be quenched to have better strength to resist failure. However, quenching generates some residual stress and deformation in the steel part which depend more on the microstructures and properties of steel governed by rapid temperature fluctuations in quenching. Therefore, to simulate the realistic quenching process computationally; a three-dimensional fluid-structure interaction model is developed for a steel part having temperature-varying properties with two liquid quenchants. The time-varying nodal temperature distribution in the part is observed and the critical regions are identified. The behavior of the residual stress and deformation are analyzed at a particular point and along particular pathways in the part. The convergence of the model is checked and validation of the model is done.

Nomenclature

α	Coefficient of thermal expansion	E	Modulus of elasticity
ρ	Density	S	Specific heat
ν	Poisson's ratio	Y	Yield strength
k	Thermal conductivity	T	Temperature

* Corresponding author. Tel.: +1-504-638-7209.
   E-mail address: psarker1@uno.edu

1. Introduction

Among different heat treatment processes, quenching is the rapid cooling of the workpiece to improve certain material properties, e.g., the microstructure, hardness, toughness, and corrosion and wear resistance by introducing martensite, a very hard form of steel crystalline structure. Since steel parts are widely used as machine components in environments where they have to withstand highly dynamic torsional and compressive stresses, they need to be quenched to have greater strength to resist failure. However, rapid heat transfer from the hot object to the quenchant causes phase transformation generating some residual stresses and deformations in the object which ultimately depend on the temperature dependent properties of the material. Therefore, it is important to observe the quenching characteristics of steel with temperature dependent properties. There are uses of different quenching media, e.g., liquids or gases [1–3]. Liquid quenchants like water and brine produce enough quench severity to have martensitic transformation. While water quenching offers hard microstructure, it also creates distortion and cracking and brine is somewhat corrosive in nature. Oil quenching does not have these disadvantages but the cooling rate is not sufficient to harden the part as required. To overcome these problems, glycol based quenchants are introduced in practice [4].

Previous works suggest that the residual stress and deformation are measured by various methods in transient analysis. Yamada [5] presented a method for solving uncoupled quasi-static thermo-elastic problems in perforated plates with prescribed temperatures. The transient thermal stress problem in a thermally and elastically orthotropic rectangular slab was investigated by Wang and Chou [6]. Nowadays, the finite element (FE) method is used to predict the residual and thermal stress in the material [3, 7–8]. The stress and deformation generated due to quenching are influenced by a number of parameters and vice versa. Sedighi and McMahon [9] investigated the effect of variation in part orientation and quenchant circulation during the quenching of steel parts to estimate the residual stresses. Kamamato et al. [10] showed that transient stresses due to quenching in large low-alloy steel shafts affected each other and were strongly related to the transformational behavior. Experimental studies of thermal stresses after quenching were also done. Investigation of the thermal stress in a viscoelastic-plastic plate was carried out experimentally by Landau et al. [11]. Xiao studied the effect of heat transfer coefficient distribution on thermal boundary conditions numerically and experimentally for optimization of aluminium and steel quenching [12].

In most of the cases in previous works, the thermal stress and deformation were determined either by static analysis or by using constant properties of the quenched part. Therefore, in this paper, a three-dimensional (3-D) fluid-structure interaction (FSI) model of a steel part with temperature dependent properties is developed to simulate the realistic quenching process by two sequentially coupled steps: heat transfer and stress analysis. The nodal time-varying temperature distributions and nodal as well as path-wise residual stress and deformation in the part are studied. The cooling rates of two different liquid quenchants are compared to each other and the critical regions are identified. The convergence of the model is checked and validation is done by numerical results presented in [11].

2. Properties of the steel part and the quenchants

The object to be quenched is a steel tube with inner radius, outer radius, and height of 1.2 mm, 2.5 mm, and 9.0 mm, respectively [13]. The steel has temperature-varying properties listed by Eqs. (1)–(12) [14], except for ν =0.3, ρ_s =7830 kg/m³, E_s =206.8e9 Pa, and Y_s = 248e6 Pa [11]. The subscript s refers to standard properties of steel at normal temperature. Two different liquid quenchants, water and 10% w/w propylene glycol (PG) aqueous solution are used as liquid quenchants [13]. The properties of the liquid quenchants at 25 °C are given in Table 1.

Thermal conductivity (W/m.K):

$$k = -0.022T + 48 \qquad\qquad T \leq 900\,°\text{C} \qquad (1)$$

$$k = 28.2 \qquad\qquad T > 900\,°\text{C} \qquad (2)$$

Specific heat (J/kg.K):

$$S = \frac{(0.004T + 3.3) \times 10^6}{\rho_s} \qquad\qquad T \leq 650\,°\text{C} \qquad (3)$$

$$S = \frac{(0.068T - 38.3) \times 10^6}{\rho_s} \qquad\qquad 650\,°\text{C} < T \leq 725\,°\text{C} \qquad (4)$$

$$S = \frac{(-0.086T + 73.35) \times 10^6}{\rho_s} \qquad 725\,°C < T \le 800\,°C \qquad (5)$$

$$S = \frac{4.55 \times 10^6}{\rho_s} \qquad T > 800\,°C \qquad (6)$$

Modulus of elasticity (Pa):

$$\frac{E}{E_s} = 1.0 + \frac{T}{2000\ln(T/1100)} \qquad T \le 600\,°C \qquad (7)$$

$$\frac{E}{E_s} = \frac{690 - 0.69T}{T - 53.5} \qquad T > 600\,°C \qquad (8)$$

Yield strength (Pa):

$$\frac{Y}{Y_s} = 1.0 + \frac{T}{900\ln(T/1750)} \qquad T \le 600\,°C \qquad (9)$$

$$\frac{Y}{Y_s} = \frac{340 - 0.34T}{T - 240} \qquad T > 600\,°C \qquad (10)$$

Coefficient of thermal expansion (/K):

$$\alpha = (0.004T + 12) \times 10^{-6} \qquad T < 1000\,°C \qquad (11)$$

$$\alpha = 16 \times 10^{-6} \qquad T \ge 1000\,°C \qquad (12)$$

Table 1: Properties of the liquid quenchants at 25 °C

Property	Water	10% w/w PG aqueous solution
Density, kg/m^3	1000	1004
Viscosity, Pa.s	0.891e–3	1.2e–3
Thermal conductivity, W/m.K	0.61	0.565
Specific heat, J/kg.K	4200	4200

3. The fluid-structure interaction model

The 3-D FSI model consists of the steel tube as the solid FE model and the liquid quenchant as the computational fluid dynamics (CFD) model, both developed by Abaqus 6.12. The analysis is run by a sequentially coupled method consisting of two steps; the transient heat transfer analysis between the tube and the quenchant and the thermal stress analysis of the tube. The heat transfer analysis couples the FE model with the CFD model to generate the temperature-time history used as an input in the second step to estimate the thermal stress. The initial temperature of the tube and the quenchants are 850 °C [12] and 25 °C, respectively, where the latter is also the sink temperature.

3.1 Physical domain

Figures 1(a) and 1(b) show the computational fluid domain for the liquid quenchant and the steel tube, respectively. The fluid domain in Fig. 1(a) has the length, width, and height of 25 mm, 20 mm, and 15 mm in X-, Y-, and Z-directions, respectively. The solid domain in Fig. 1(b) has the dimensions as described in the property section. Figure 2 describes the longitudinal cross-section of the tube about the YZ-plane with axial and radial pathways AB (from node 52 to node 25) and CD (from node 68 to 27), respectively, to see the nature of variations of the stress and deformation along the normalized distance. The normalized distance is a dimensionless distance defined as the ratio of any distance from the start of the path to the total length of the path. To observe the behaviour of time-varying temperature, two nodes J (on plane LFGM) and K (on plane IHGF) are randomly chosen in the tube. Node E is the intersection as well as the midpoint of paths AB and CD. Table 2 gives the coordinates of all the nodes described in Fig. 2.

Fig. 1. Computational domains for the (a) liquid quenchant; (b) solid steel tube

Fig. 2. Locations of nodes and paths of analyses

Table 2: Coordinates of the nodes of Fig. 2

Node label	X-coordinate, mm	Y-coordinate, mm	Z-coordinate, mm
J (2)	−1.85	0	9
E (24)	0	−1.85	4.5
B (25)	0	−1.85	9
D (27)	0	−2.5	4.5
A (52)	0	−1.85	0
C (68)	0	−1.2	4.5
K (2471)	0	2.067	0.783

3.2 Interaction and boundary conditions

The interaction surface is the common surface between the tube and the quenchant. For the tube, it is the whole surface area except for the bottom surface Q in XY-plane shown in Fig. 1(b). The boundary conditions for both the fluid and the solid domains of Fig. 1 are listed in Tables 3 and 4, respectively. For fluid domain the boundary conditions are specified in terms of velocity or pressure and for solid domain, they are expressed in terms of displacement and rotation. In Table 3, v indicates the velocity with subscripts x, y, and z meaning corresponding components in X-, Y-, and Z-directions, respectively. In Table 4, u and θ indicate the displacement and the rotation of the tube, respectively, with same meaning of the subscripts of Table 3. For the solid tube domain of Fig. 1(b), the bottom surface Q always remains in the XY-plane and point P (X= −2.5 mm, Y= 0 mm, Z= 0 mm) is fixed.

Table 3: Boundary conditions for fluid domain

		Boundary conditions			
		Velocity, m/s			
Name	Surfaces	v_x	v_y	v_z	Pressure, Pa
In-flow	ABDC	1	0	0	-
Top-flow	ABFE	1	0	0	-
Side-flow	BFGD	1	0	0	-
Side-flow	AEHC	1	0	0	-
Out-flow	EFGH	-	-	-	0
No-slip	CDGH+ I+ J+ K+ L	0	0	0	-

Table 4: Boundary conditions for solid domain

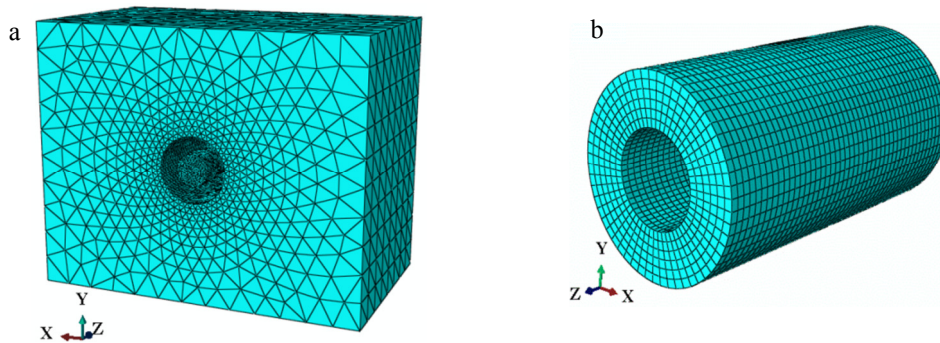|		Boundary conditions					
		Displacement, m			Rotation, degrees		
Name	Surfaces/Points	u_x	u_y	u_z	θ_x	θ_y	θ_z
Bottom surface	Q	-	-	0	-	-	-
Fixed point	P	0	0	0	0	0	0

3.3 Mesh generation

Fig. 3. (a) The meshed fluid domain; (b) the meshed solid steel tube

Figure 3(a) shows the meshed fluid domain with the finest element size of 2 mm [13] with a high mesh density at inner and outer edges of the cavity, meshed by FC3D4 (four-node, linear, fluid-tetrahedron) elements. Figure 3(b) represents the meshed FE model of the tube with the finest element size of 0.2 mm [13]. After meshing, the tube has 15,456 elements and 18,424 nodes. DC3D8 (eight-node linear heat transfer brick) elements are used for heat transfer step and C3D8R (eight-node, linear brick, reduced integration) elements are used to calculate the 3-D stress.

4. Results and discussions

4.1 Model validation, convergence study, and the cooling curve
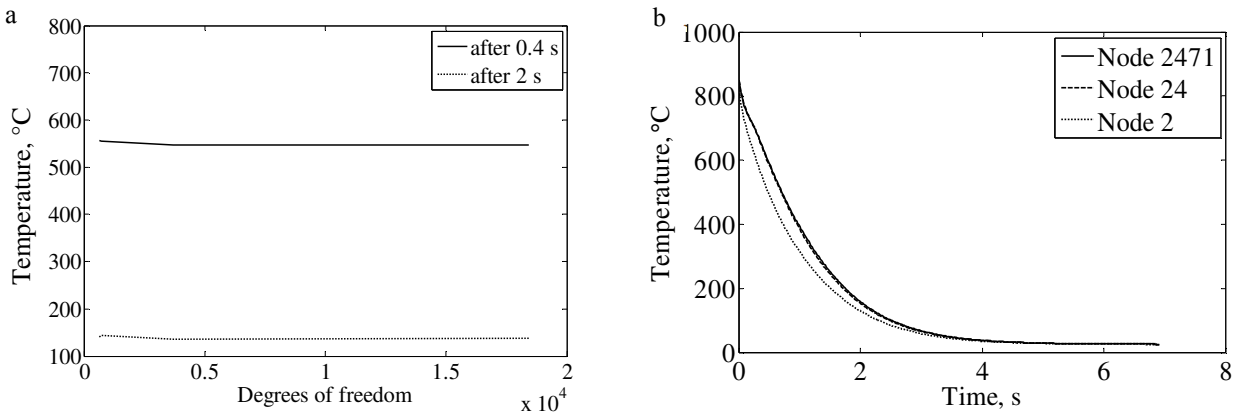
Fig. 4. Variations of the (a) temperatures of node 24 with degrees of freedom; (b) temperature of nodes 2, 24, and 2471 with time for water

For validating the FE model, the residual stress computed by Landau et al. [11] for an infinite plate with one-dimensional (1-D) heat transfer is compared with that of the developed FE model. The maximum variation of the stress computed by two models (Ref. [12] and developed FE model) is 8%. As the FE model with 1-D heat transfer works well, the current 3-D model for the tube is investigated for further analysis. Figure 4(a) shows the variations of the temperatures of node 24 versus the degrees of freedom (DOF) at two different time steps for the constant property quenching analysis [13] showing that the temperature becomes flattened as the DOFs increase meaning that the solution is already converged. Since, the constant property model confirmed mesh independence; it is justified to assume that this variable property model has also become mesh independent with the aforesaid mesh sizes. Figure 4(b) shows the cooling curves of nodes 2, 24, and 2471 for water quenching indicating that the temperature of each node decreases exponentially with time. The cooling rates of all the curves are just the slopes of the curves.

4.2 Residual stress and deformation analysis
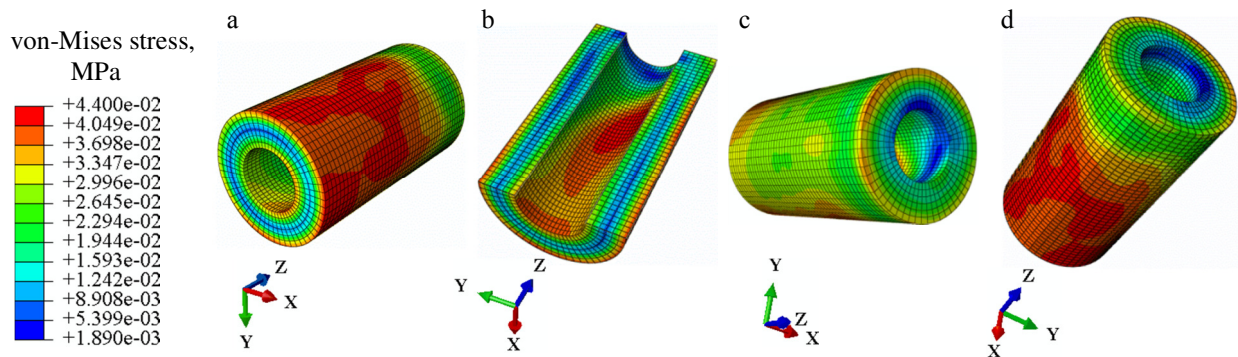
Fig. 5. Distributions of the von-Mises stress in (a) the whole steel tube; (b) the cross-sectional half of the tube in downstream flow direction; (c) the outer surface of the tube in upstream flow direction; (d) the outer surface of the tube in downstream flow direction
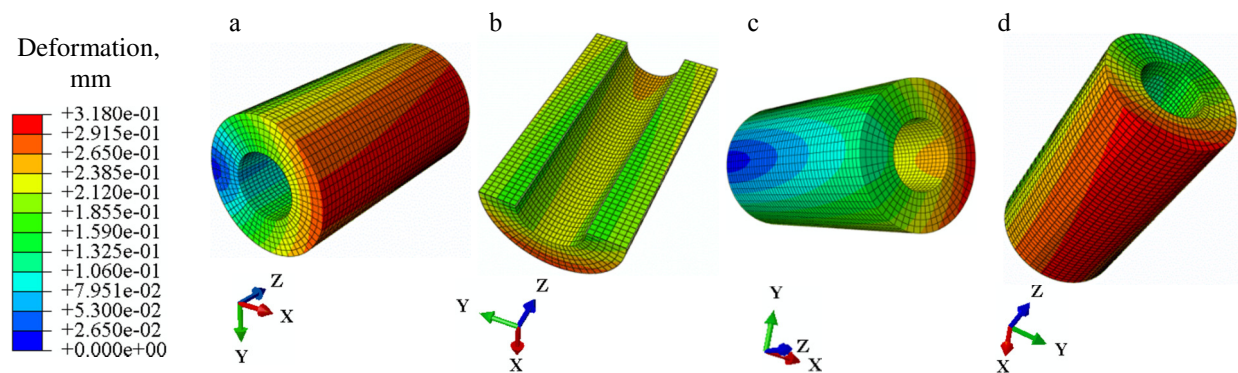

Fig. 6. Distributions of the deformation in (a) the whole steel tube; (b) the cross-sectional half of the tube in the downstream flow direction; (c) the outer surface of the tube in upstream flow direction; (d) the outer surface of the tube in downstream flow direction

Figures 5(a) through 6(d) describe the deformed contour of the steel tube for PG quenching in terms of the von-Mises stress and deformation. From Fig. 5, the highest von-Mises stress generated in the tube for PG quenching is 44 kPa which occurs in the lower-half of the outer surface and the mid-internal surface of the tube in the downstream flow direction. The top surface of the tube shows relatively smaller stress near the vicinity of the internal edge in Figs. 5(b), 5(c), and 5(d). From Fig. 5(c), the outer surface of the tube in the upstream direction of flow does not show much variation of stress and the intensity of the stress is medium. This is because the cooling environments in the upstream and downstream directions of the tube are different. The bottom surface of the tube shows low level stress in between the inner and the outer edges of the tube as this surface is not radially constrained to move. From Fig. 6(a), the deformation on the outer surface of the tube in the downstream flow direction varies both radially and axially with the maximum value of 0.32 mm at the outer top surface. Figures 6(b), 6(c), and 6(d) reveal that as one goes axially down from top to bottom of the tube, the deformation gradually reduces for both the inner and the outer curved surfaces. This is because the top surface of the tube is comparatively free to move vertically than the bottom surface where the XY-plane is constrained to have no deformation along Z-direction.

The time-varying behaviors of the von-Mises stresses and deformations at node 24 for water and PG quenching are depicted in Figs. 7(a) and 7(b). From Fig. 7(a), starting from zero, all the curves for water and PG quenching follow a sharp rise of stresses up to 13.99 MPa and 14.32 MPa, within 0.76 s and 0.64 s, respectively. After that, they start decaying from the peak stresses exponentially and get flattened, ending with stresses of 18.9 kPa and 8 kPa for water and PG, respectively. From Fig. 7(b), the gap between the curves increases with the water deformation curve always at the top of that of PG. Greater quench severity of water creates higher deformation (0.39 mm) compared to PG (0.19 mm) at the end. Comparing Figs. 7(a) and 7(b), a trend of decreasing stress in Fig. 7(a) is followed by increasing deformation in Fig. 7(b).
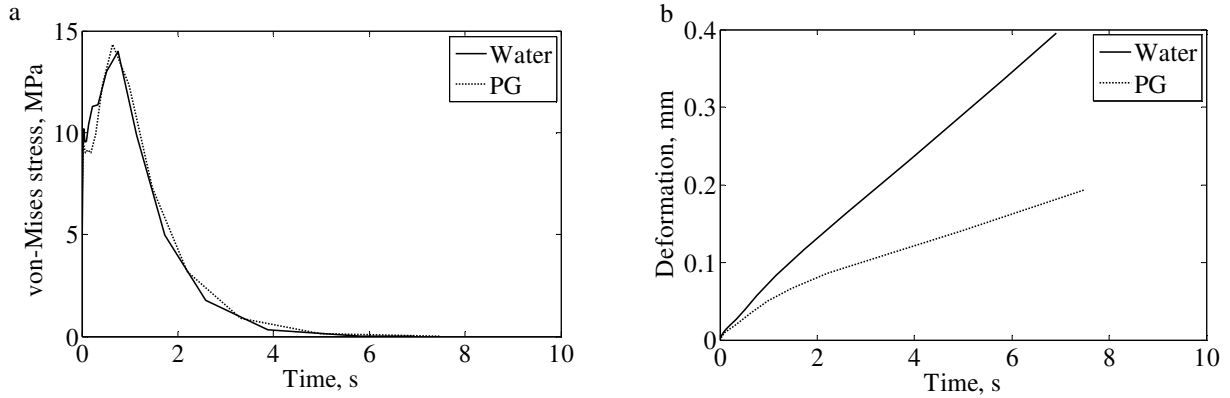
Fig. 7. Time-variations of the (a) von-Mises stress; (b) deformation of node 24 for different quenchants
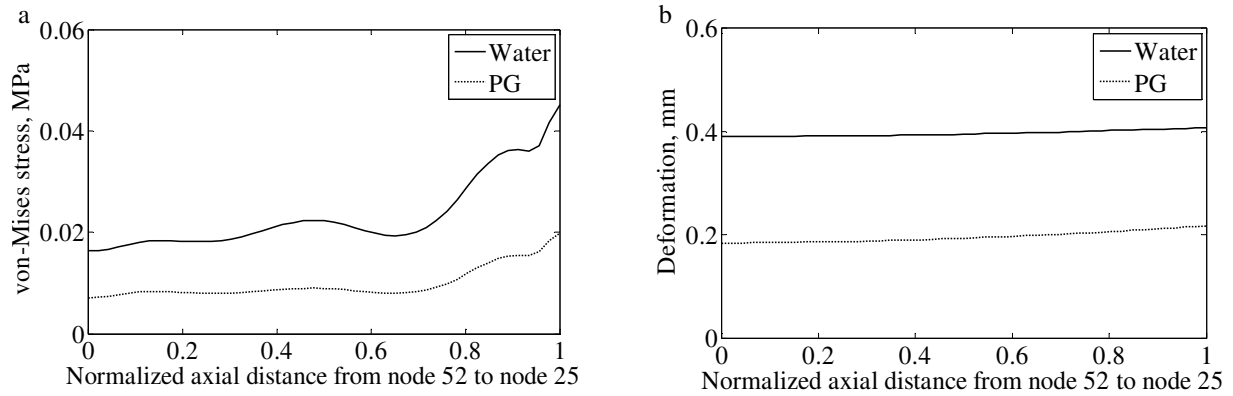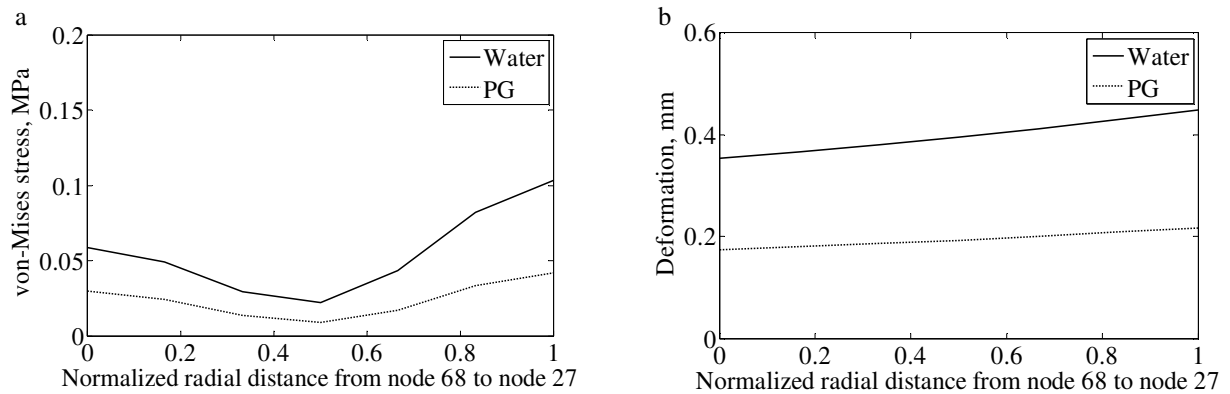

Fig. 8. Variations of the (a) von-Mises stress; (b) deformation axially along path AB from node 52 to node 25

The axial variations of the von-Mises stress and deformation along path AB (Fig. 2) are analyzed in Figs. 8(a) and 8(b), respectively. From Fig. 8(a), the stress along path AB fluctuates harmonically for both quenchants. However, the overall trend gives the indication that axially, the stress is on the increase with higher stress for water quenching than that of PG quenching. The stresses at point B are 45.1 kPa and 19.8 kPa for water and PG quenching, respectively. From Fig. 8(b), the deformations increase slightly from point A to point B for both quenchants with water deformation curve at the top. The magnitudes of deformations at point A by water and PG quenching are 0.39 mm and 0.18 mm, respectively, and for point B, they are 0.41 mm and 0.22 mm, respectively.

Fig. 9. Variations of the (a) von-Mises stress; (b) deformation radially along path CD from node 68 to node 27

Figure 9(a) gives the variation of the von-Mises stress along the radial path CD (Fig. 2). Unlike the axial stress distribution, it shows a gradual decrease of stresses from node C to node E for both quenchants. The magnitudes of stresses at node C are 58.4 kPa and 30 kPa for water and PG, respectively. After reaching the lowest stress levels at point E, they again start rising from there and end up with 103.5 kPa and 41.9 kPa at node D for water and PG, respectively. Lastly, the trend of radial deformation along CD in Fig. 9(b) also shows that the deformation created by water is always greater (0.35 mm at C and 0.45 mm at D) than that of PG (0.17 mm at C and 0.22 mm at D).

5. Conclusions

In this analysis, a three-dimensional fluid-structure interaction model is developed to observe the quenching characteristics of a steel tube having temperature dependent properties with two different liquid quenchants; water and propylene glycol. The following outcomes are generalized from this variable property quenching analysis:

1. If one considers only the cooling capacity or severity of quenching, water is better for its least quenching time. However, as a quenchant, propylene glycol is better as it offers least stress and deformation while quenching.

2. The selection of a suitable quenchant depends on the required quench severity, the wetting property, and the viscosity of the quenchant including the shape, dimension, and composition of the object to be quenched.

3. The stress and deformation distributions in the tube are similar for both water and PG quenching and vary only in magnitudes. The highest stresses developed by water and PG quenching are 120 kPa and 44 kPa, respectively, on the lower-half of the outer surface and on the inner surface of the tube in the downstream flow direction. The deformation also shows similar characteristics. The greatest deformations are 0.63 mm and 0.32 mm, for water and PG quenching, respectively, on the outermost edge on the top surface of the tube in the downstream flow direction.

4. A faster cooling is always preferable but it generates more stress and deformation. Therefore, to ensure optimum stress and deformation, a suitable quenchant needs to be selected to maintain a balance among achieving desired material properties and other design parameters.

References

[1]   I. Elkatatny, Y. Morsi, A.S. Blicblau, S. Das, E. Doyle, Numerical analysis and experimental validation of high pressure gas quenching, International Journal of Thermal Sciences 42(4) (2003) 417–423.
[2]   Y. Jintang, Q. Haiduan, L. Gongfa, Z. Xiaoliang, Numerical simulation of the quenching process of U71Mn rail–head based on ANSYS software, Proceedings of the International Conference on Measuring Technology and Mechatronics Automation, 2 (2010) 811–816.
[3]   M. Toparli, T. Aksoy, Calculation of residual stresses in cylindrical steel bars quenched in water from 600 °C, Proceedings of AMSE Conference, New Delhi, India, 4 (1991) 93–104.
[4]   B. Bautista, D. Diaz, H. Garcia, Conversion and use of polymer quenchants in integral quench furnace applications, Proceedings of the First International Conference on Quenching and Control of Distortion, Chicago, IL, USA, 1992.
[5]   K. Yamada, Transient thermal stresses in an infinite plate with two elliptic holes, Journal of Thermal Stresses, 11(4) (1988) 367–379.
[6]   H.S. Wang, T.W. Chou, Transient thermal stresses analysis of a rectangular orthotropic slab, Journal of Composite Materials, 19(5) (1985) 424–442.
[7]   Y. Fa-Rong, W. Shang-li, Transient temperature and residual stress fields in axisymmetric metal components after hardening, Journal of Material Science and Technology, 1(10) (1985) 851–856.
[8]   Z. Li, R.V. Grandhi, R. Srinivasan, Distortion minimization during gas quenching process, Journal of Materials Processing Technology, 172(2) (2006) 249–257.
[9]   M. Sedighi, C.A. McMahon, The influence of quenchant agitation on the heat transfer coefficient and residual stress development in the quenching of steels, Proceedings of the Institution of Mechanical Engineers, Part B: Journal of Engineering Manufacture, 214(7) (2000) 555–567.
[10]   S. Kamamato, T. Nihimori, S. Kinoshita, Analysis of residual stress and distortion resulting from quenching in large low-alloy steel shafts, Journal of Material Science and Technology, 1(10) (1985) 798–804.
[11]   H.G. Landau, J.H. Weiner, E.E. Zwicky Jr., Thermal stress in a viscoelastic-plastic plate with temperature dependent yield stress, Journal of Applied Mechanics, 27(2) (1960) 297–302.
[12]   B. Xiao, Numerical modeling and experimental investigation for optimization in quenching processes of aluminum and steel parts, Ph.D. dissertation, Worcester Polytechnic Institute, 2010.
[13]   P. Sarker, U.K. Chakravarty, Analysis of the residual stress and deformation in a steel tube due to quenching process using different media, Proceedings of the ASME International Mechanical Engineering Congress and Exposition, Montreal, QC, Canada, 2014.
[14]   V. Kodur, M. Dwaikat, R. Fike, High-temperature properties of steel for fire resistance modelling of structures, Journal of Materials in Civil Engineering, 22(5) (2010) 424–434.

6th BSME International Conference on Thermal Engineering (ICTE 2014)

Processing and Mechanical Characterization of Graded and Non-graded Nanoclay Composites

Shoumya Nandy Shuvo[a], Kazi Md. Shorowordi[b]*

aPostgraduate Student, BUET, Dhaka-1000, Bangladesh
bAssistant Professor, BUET, Dhaka-1000, Bangladesh

Abstract

In this research, nanoclay reinforced polyester nanocomposites were developed with a semi-commercial process. Two types of nanoclays viz. graded and non-graded nanoclay were used as reinforcements. Each of the nanoclay was added 1 wt. % in polyester separately and the effects of the addition of nanoclay on the polyester were studied by mechanical characterization. Tensile and flexural strength were measured by using an Instron Universal Testing Machine. Hardness of the developed nanocomposites was measured by a Shore Hardness Tester. The fracture surfaces were investigated by Scanning Electron Microscope (SEM). It is found that the modulus and strength of graded nanoclay reinforced nanocomposite is higher than that of the unreinforced polyester and non-graded nanoclay reinforced nanocomposite. The flexural strength is also found to be higher in the graded nanoclay composites as compared to the unreinforced polyester and non-graded nanoclay reinforced nanocomposite. The hardness of unreinforced polyester and both the nanocomposites are almost same. The fracture morphology of the unreinforced polyester and reinforced nanocomposites and its correlation with mechanical properties are also discussed.

* Corresponding author. Tel.: +01711-453647.
   E-mail address: shoum_nandy40@hotmail.com

1. Introduction

Nanocomposites have courted and enticed attention in recent years because of improved mechanical, thermal, solvent resistance and fire retardant properties compared to the pure or conventional composite materials. Therefore, much work has focused on developing polymer/clay nanocomposites using various polymers which add to the lure of advancement of modern materials. In the simplest case, appropriately adding nanoparticulates to a polymer matrix can enhance its performance, often dramatically, by simply capitalizing on the nature and properties of the nanoscale filler [1]. This strategy is particularly effective in yielding high performance composites, when good dispersion of the filler is achieved and the properties of the nanoscale filler are substantially different or better than those of the matrix. An example of this would be reinforcing a polymer matrix by much stiffer nanoparticles of ceramics, clays, or carbon nanotubes [2-3]. By the addition of the nanofillers, the improvement in mechanical properties not only is limited to stiffness or strength, but it is also extended to improve the time-dependent properties [4]. Alternatively, the enhanced crystallization behaviour under flow conditions and other physical properties of high performance nanocomposites is mainly due to the high aspect ratio and/or the high surface area of the fillers, since nanoparticulates have extremely high surface area to volume ratio when good dispersion is achieved [5-7]. Nanoparticle dispersion in the polymer matrix is a key issue, which limits the applicable particle volume fraction and therefore also the multi-functionality of the composite material.

Nanoclay is one of the most affordable materials that have shown promising results in polymers. The clays used for the preparation of nanoclays or organoclays belong to smectite group or montmorillonite clays. Organophilic clay (nanoclay) can be obtained by simply the ion-exchange reaction of hydrophilic clay with an organic cation such as an alkyl/aryl ammonium, phosphonium or imidazolium cations in aqueous solution or in the solid state. The inorganic ions are exchanged with more voluminous organic onium cations. When the solubility of quaternary salts is low, water-alcohol mixtures are often used as a solvent. The ion exchange reaction has two consequences; first, the gap between the single sheets is widened, enabling organic cations chain to move in between them and second, the surface properties of each single sheet are changed from being hydrophilic to hydrophobic or organophilic [8-9]. Montmorillonite consists of ~ 1 nm thick aluminosilicate layers surface-substituted with metal cations and stacked in ~ 10 µm-sized multilayer stacks. The stacks can be dispersed in a polymer matrix to form polymer-clay nanocomposite. Within the nanocomposite, individual nm-thick clay layers are fully separated to form plate-like nanoparticles with very high (nm x µm) aspect ratio. Even at low nanoclay loading (a few weight %), the entire nanocomposite consists of interfacial polymer, with majority of polymer chains residing in close contact with the clay surface. Potential benefits include increased mechanical strength, decreased gas permeability, superior flame-resistance, and even enhanced transparency when dispersed nanoclay plates suppress polymer crystallization [10]. Thus the present study has therefore been taken to study the effect of graded and non-graded nanoclay on polyester.

2. Experimental Procedure

The materials in this experiment were pure polyester, graded nanoclay (nanoclay nanomer 1.31 PS, montmorillonite clay surface modified with 15-35 wt% octadecylamine and 5 wt% aminopropyltriethoxysilane), non-graded nanoclay which is basically non-processed and non-modified clay collected from local areas and a hardener which is methyl ethyl ketone peroxide hardener (molecular formula: $C_8H_{18}O_6$, molar mass: 210.22 g mol^{-1}, appearance: colorless liquid, density: 1.170 g cm^{-3}).

First of all, raw samples of non processed clay were obtained from Chuyadanga local areas for the accomplishment of non-graded nanoclay. This kind of clay contains nano-size particles as well as micro-sized particles and even larger particles. So it was a necessity to have them refined and separated. The clay was then processed in a semi-commercial technique for it to be at an approximate nano level. A portion of the lumps of clay was taken in a funnel and appropriate amount of water was added in the clay. Then significant time was allowed for the large size clay to settle. The small size clay was then filtered through a 100 micron sieve and those that passed through the sieve were collected in a bucket. The particles passing through the sieve means that they are finer and therefore collected. The procedure was then repeated with the collected clay-water mixture so that finer and finer

clay particles can be obtained. The whole process was then repeated for other portions of the lumps of clay. After 3-4 days the prepared non-graded nanoclay was collected from the bucket and was kept a drying oven at 110°C for 24 hrs. The clay was then taken out of the oven and ground in a mortar for ensuring finer particles. The non-graded clay was then stored in an air tight container.

Liquid polyester was selected as matrix material for this study and collected from local market. The dimension of the casting dies were 100 mm in diameter and 6 mm in thickness. First of all, pure polyester samples were produced for standard comparison. Usually air/gas remains dissolved into the liquid polyester. Before casting the liquid polyester and the nanoclay into the dies was made gas/air free by a vacuum process. Then hardener (methyl ethyl ketone peroxide) of required proportion was added inside the gas free liquid polyester and stirred properly for obtaining a uniform mixture. The mixture was again evacuated putting the beaker inside the vacuum chamber for removing air and the beaker was taken from the chamber, and the pasty mass was cast into die of required shape. For preparing nanocomposites, 1 wt.% of graded and 1 wt.% non-graded nanoclay was added to the polyester separately and the mixture was stirred properly to get uniform distribution of the reinforcing particles.

More than eight samples of pure polyester and each group of composites were made through die cast method. The rectangular samples were then machined as ASTM standard tensile test samples. The final dimensions of the tensile test samples were 100 mm x 12 mm x 6 mm with gauge length 30 mm. For performing bend test, casting samples were machined to produce a rectangular shape of dimensions 5 mm thickness, 13 mm width with span length of 80 mm.

After tensile tests, fracture surfaces were cut for fractographic analysis under the Field Emission SEM. To avoid charging effect, the fracture surfaces of all samples were coated by gold sputtering technique. Under SEM, various fracture features were investigated.

3. Results and Discussion

Tensile properties of pure polyester (P), polyester reinforced with non-graded nanoclay (P+NGNC) and polyester reinforced with graded nanoclay (P+GNC) are shown in Table 1. It is observed that the tensile strength and modulus of pure polyester decrease by about 30% with the addition of non-graded nanoclay. The reason behind the decrease in strength of polyester with the addition of non-graded nanoclay may be attributed due to the agglomeration of nano particles and also due to the inhomogeneous mixture between agglomerated clay particles and polyester. However, an opposite result has been achieved when graded nanoclay was added to pure polyester as reinforcement. The maximum tensile strength and modulus has increased by about 10% compared to that of pure polyester. This is because all the clay particles are of same size at a nano level as they are graded and processed in a commercial way. Therefore, this has resulted in a larger surface area than that of any other reinforcement and therefore leading to a very efficient stress transfer mechanism, hence resulting in a higher strength and modulus. The trend is consistent with the results reported by others. According to Kojima et al., a region where the polymer chains are restricted in mobility contributes to the improvement of the tensile modulus in a polymer–clay hybrid [11].

Table 1: Tensile properties of pure polyester, polyester reinforced with non-graded nanoclay and polyester reinforced with graded nanoclay.

Samples	Maximum tensile strength (MPa)	0.2% offset yield strength (MPa)	Modulus (MPa)
P	47.9	32.6	4728
P + NGNC	32.8	23.1	3181
P + GNC	52.7	29.3	5342

Table 2 shows flexural strength of polyester, polyester reinforced with non-graded nanoclay and polyester reinforced with graded nanoclay. From the table, it can be observed that the flexural strength of pure polyester decreases by about 5% with the addition of non-graded nanoclay in polyester. According to the type of the filler, it can be suggested that the hydrophilic unmodified nanoparticles cannot be dispersed appropriately and generally agglomerates in the resin phase. This phenomenon causes the stress to be concentrated on particular points in the

resin phase and the crack to spread easily through the unfilled parts of matrix resin. This can be the main reason for crack propagation that leads to matrix fracture and reduction in flexural strength.

But when graded nanoclay is added in pure polyester as reinforcing particles, flexural strength is found to increase (about 15%) significantly. This increase may be attributed to the fact that graded nanoclay provides appropriate separation and dispersion of the particles in the resin matrix, especially in nanoscale, which plays an important role in the physical characteristics of resin-based materials. Modifications of nanoparticles can efficiently enhance their dispersion. Swelling of the grafted polymeric chains on the graded nanoclay particles may reduce their density and facilitate their distribution in the resin phase by making them polarized. This uniform dispersion in nanoscale prevents crack propagation and causes a significant improvement in flexural strength properties,

Table 2: Flexural strengths of polyester, polyester reinforced with non-graded nanoclay and polyester reinforced with graded nanoclay.

Samples	Flexural Strength (MPa)
P	82.1
P + NGNC	78.8
P + GNC	94.6

The hardness of pure polyester, polyester reinforced with non-graded nanoclay and polyester reinforced with graded nanoclay are presented in Table 3. From this table, it is seen that the hardness of unreinforced polyester and both the nanocomposites are almost same. This is because the resistance to withstand indentation did not increase upon addition of nanoclay in the polyester.

Table 3: Hardness of polyester, polyester reinforced with non-graded nanoclay and polyester reinforced with graded nanoclay.

Sample	Hardness (Shore)
P	96.1
P + NGNC	97.1
P + GNC	97.4

The fracture surfaces of pure polyester, polyester reinforced with non-graded nanoclay and polyester reinforced with graded nanoclay are shown in Fig. 1. No particles or impurities are observed in pure polyester as it is virgin polyester (Fig. 2a). It is also seen from Fig. 2a that the fracture initiation occurs in the direction of tensile loading and the mode of fracture is ductile type. The fracture surface of non-graded reinforced polyester composite shows that there exists some decohesion or debonding between agglomerated particles and polyester (Fig. 2b). It is thought that this debonding during tensile loading is responsible for the decrease in tensile strength. Fig. 2c shows the fracture surface of graded nanoclay reinforced polyester composite. Nanoclay particles, being too small and well dispersed are not seen under the Scanning Electron Microscope. But it clearly indicates that the nature of the fracture is brittle as there is no debonding or cup and cone observed, rather fracture occurs at a single leap, viz., it is a brittle fracture. The fractography analysis is supportive with the mechanical properties where tensile and flexural strengths have increased upon addition of graded nanoclay.
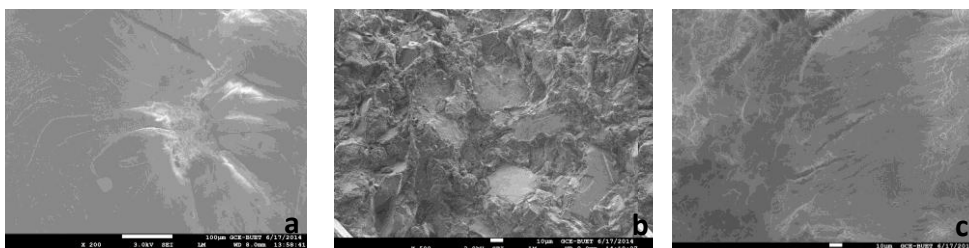

Fig. 1: SEM images of the fracture surface of (a) pure polyester, (b) non-graded nanoclay reinforced polyester composite and (c) graded nanoclay reinforced polyester composite.

4. Conclusions

The present study has been undertaken to investigate the effects of graded nanoclay and non-graded nanoclay on polyester and following conclusions can be drawn.

1. Upon addition of non-graded nanoclay to pure polyester, the tensile strength and modulus decreases from by about 30%.

2. When graded nanoclay was added to pure polyester as reinforcement, the strength and modulus has increased by about 10% compared to that of pure polyester.

3. Flexural strength of pure polyester is higher than that of polyester reinforced with non-graded nanoclay. But when graded nanoclay was used as reinforcing particles, flexural strength has increased by about 15%.

4. According to fractographic analysis, fracture of pure polyester is found to be ductile type while fracture of graded nanoclay reinforced polyester composite is brittle type.

Acknowledgements

References

[1] Manias, Evangelos (2007).”Nanocomposites: Siffer by design”. Nature Materials 6 (1): 9-11, doi: 10.1038/nmat1812, PMID 17199118.

[2] Mai, Y, Z. Yu, (2006). Y. Mai, Z. Yu, ed. Polymer Nanocomposites. Woodhead Publ.ISBN 978-1-85573-969-7.

[3] T. J. Pinnavaia, G. W. Beall (eds.), "*Polymer-Clay Nanocomposites*", Wiley, 2001;ISBN 978-0-471-63700-4.

[4] Zandiatashbar, Ardavan, Picu, Catalin R., Koratkar, Nikhil (2012). "Control of Epoxy Creep Using Graphene". *Small* 8 (11): 1676–1682. doi:10.1002/smll.201102686.

[5] Patil, N., Balzano, L, Portale, G. and Rastogi, S. (2010). "Influence of shear in the crystallization of polyethylene in the presence of SWCNTs". *Carbon* 48 (14): 4116. doi:10.1016/j.carbon.2010.07.022.

[6] Chan, M; Lau, K; Wong, T; Mei-po Ho, Hui, David; ”Mechanism of reinforcement in a nanoclay/polymer composite”, J. of Elsevier, ”Composites Part B: Engineering”, Volume 42, Issue 6, September 2011, Pages 1708–1712.

[7] Sotirou, Georgios A.; Blattmann, Christoph O.; Pratsinis, Sotiris E. (2013). "Flexible, multifunctional, magnetically actuated nanocomposite films". *Advanced Functional Materials* 23 (1): 1616–3028. doi:10.1002/adfm.201201371.

[8] Atai M, Solhi L, Nodehi A, Mirabedini SM, Kasraei S, Akbari K. PMMA-grafted nanoclay as novel filler for dental adhesives. Dent Mater. 2009;25:339–47.

[9] Bowen R., “Effect of particle shape and size distribution in a reinforced polymer”, J. of Am Dent Assoc.1964;69:481–95.

[10] Li, X. and Ha, C.-S., 2001. Nanostructure of EVA / Organoclay Nanocomposite: Effects of Kinds of Organoclays and Grafting of Maleic Anhydried onto EVA, *J.Appl.Polym.Sci*., 87: 1901-1909.

[11] Kojima, Yoshitsugu; Kawasumi, Masaya; Okada, Akane; Fukushima, Yoshiaki; Kurauchi, Toshio; Kamigaito, Osami; Usuki, Arimitsu; (1993). "Synthesis of nylon 6-clay hybrid".*Journal of Materials Research* 8 (5): 1179. doi:10.1557/JMR.1993.1179.

6th BSME International Conference on Thermal Engineering (ICTE 2014)

Processing and Performance Evaluation of Amine Functionalized Graphene Nanoplatelet (GNP) Reinforced Epoxy Composite

Md Mahmudur R. Chowdhury[a], Mohammad K. Hossain[a, *], Mahesh Hosur[b], Shaik Jeelani[b], Nydeia W Bolden[c].

[a]Department of Mechanical Engineering, Tuskegee University, Tuskegee, AL 36088, USA

[b]Department of Materials science and Engineering, Tuskegee University, Tuskegee, AL 36088, USA

[c]Air Force Research Laboratory Munitions Directorate, Eglin AFB, FL 32542

Abstract

A systematic study has been conducted on the processing and characterizing the epoxy polymer composite with enhanced properties through the optimization of the graphene nanoplatelet (GNP). This extensive research has been focused on the reinforcing effect of the GNP and amine functionalization effect of the GNP on mechanical, viscoelastic, and thermal properties of the epoxy resin-EPON 828 composite. Amine functionalized GNPs were infused in EPON 828 at different loadings including 0, 0.1, 0.2, 0.3, 0.4, and 0.5 wt% as reinforcing agent. GNPs were infused into Epon 828 resin using a mechanical stirrer followed by a high intensity ultrasonic liquid processor for better dispersion. After the sonication, the mixture was placed in a three roll milling processor for 3 successive cycles at 140 rpm, with the gap spacings incrementally reduced from 20 to 5 μm, to obtain the uniform dispersion and proper exfoliation of GNP throughout the resin. Epikure 3223 curing agent was then added to the modified resin and mixed using a high-speed mechanical stirrer. The reinforcing effect of the amine functioanalized GNP on the epoxy was characterized through mechanical, viscoelastic, and thermal analyses. The mechanical properties were determined through flexure test according to the ASTM standard. Dynamic mechanical analysis (DMA) was performed to analyze the viscoelastic and thermal performances of the composite. In all cases, the 0.4 wt% GNP infused epoxy nanocomposite exhibited the best properties. The 0.4 wt% GNP-loaded epoxy sample showed 20% and 40% improvement in flexure strength and modulus, respectively. Moreover, 16% improvement in the storage modulus and 37% decrease in the coefficient of thermal expansion were observed for the GNP reinforcement. Scanning electronic microscopy (SEM) micrographs exhibit smooth fracture surface for the neat sample, whereas the roughness of surface increases due to the GNP incorporation. This is the indication of the change in the crack propagation.

Keywords: Graphene Nanoplatele; Mechanical properties; Viscoelastic properties; Amino functionalized; DMA; TMA.

1. Introduction

In the last two decades, researchers have successfully enhanced the matrix properties by incorporating various nanoparticles such as clays, carbon nanofibers, silicon carbide and many more into epoxy resin composites to improve the overall properties as well as reduce cost of fiber reinforced composites. Among them carbon nanotube (CNT) have already been proven to be a potential candidate for matrix modification because of its exceptional strength and stiffness, high specific surface area, and high aspect ratio [1-3]. However, due to the higher production cost of CNTs [2] the mass production of CNT based multifunctional composite materials is also expensive. On the other hand, graphene nanoplatelets (GNPs) having a two dimensional structure are composed of several layers of graphite nanocrystals stacked together [4-5]. GNP has been providing supreme reinforcement and conducting fillers along with greatly improved mechanical properties due to their planar structure and ultrahigh aspect ratio. The GNP is the novel nanofiller due to its exceptional functionalities, high mechanical strength, chemical stability, abundance in nature, and cost effectiveness. Moreover, it possesses an extremely high-specific surface area which carries a high level of transferring stress across the interface and provides higher reinforcement than carbon nanotubes. Superior properties of graphene in comparison with the polymers are elucidated in polymer/graphene nanocomposites [6-9]. Compared to the mechanical and electrical properties of clay or other carbon-filler based polymer nanocomposites graphene based polymer nanocomposites have far better properties [10-11]. In terms of thermal and electrical conductivity, graphene behaves as a better nanofiller than CNTs [12-14]. Very recently Koratkar at el. followed a similar approach to investigate the mechanical properties of epoxy/GP nanocomposites. They observed an improvement of epoxy fracture toughness from 0.97 MPam$^{1/2}$ to 1.48 MPam$^{1/2}$ at 0.1 wt% filler fraction [15]. Investigating the graphene epoxy composites at low filler content of 0.1 wt% showed a significant increase of 31% in modulus and 40% in fracture toughness [16]. Yasmin at el [17] proposed a method in which they prepared epoxy/graphite nanocomposites by mixing epoxy with graphite in solvent. This demonstrated a use of 4 wt% in graphite causes Young's modulus to be increased by 10% and glass transition temperature (T_g) from 143 °C to 145 °C. If the mixing process is promoted by sonication and shear mixing then 1 wt% GP increase causes Young's modulus an increase of 15% which is accompanied by a reduction of tensile strength [18]. The surface modification of nanofillers helps rejuvenate the interaction between the matrix and nanofillers ensuing better dispersion quality and high performances. Better overall properties and enhanced interface between two components of the polymer

matrix can be obtained by applying modification through chemical bonding [19-20]. Amino functionalization of the carbon nanotube (CNT) has been extensively used to improve interfacial interaction with epoxy matrices [21-23]. In analogy to CNTs, covalent bond formation between epoxy resin and amine group present on the amino functionalized GNP surface is anticipated [24-25].

In this study, amino functionalized GNP reinforced epoxy nanocomposites were manufactured using the combination of sonication and the 3 roll mixing process. Flexure test, DMA, and thermo-mechanical analysis (TMA) were performed to investigate the effect of GNP on the mechanical and thermo-mechanical properties of carbon fiber/epoxy composites.

2. Experimental

The matrix used in this study is a two part system. Part A is Epon 828 (Diglycidyl Ether of Bisphenol A), and Part B is Epicure 3223, a Diethylenetriamine (DETA) used as a curing agent of epoxy resin, obtained from Miller Stephenson Chemical Company, Danbury, GNPs functionalized with amine groups ($-NH_2$) was received from Cheap Tubes Inc, Vermont, USA.

At first, pre-calculated amount of GNPs (0.1, 0.2 0.3, 0.4 or 0.5 wt%) were mechanically mixed with epoxy resin Part-A by a mechanical stirrer for 4-5 minutes . The mixture was then put into a sonicator for 1 h and passed through the three rollers to further improve the dispersion of GNPs. The GNP/epoxy mixture was then mixed with the curing agent Epikure 3223 according to the stoichometric ratio (Part A: Part B = 12:1). The mixture was then placed in a vacuum oven at 40 °C for 10 minutes to ensure the complete removal of entrapped bubbles and thus reduce the chance of void formation. The prepared resin mixture was then poured in a rubber mold to prepare the samples for characterization according to ASTM standards. Similarly, neat epoxy samples will be fabricated to compare with the nanophased samples.

Flexural test was performed under a three-point bend configuration on a Zwick Roell Z 2.5 testing unit according to the ASTM D 790- 02 standard. DMA was performed with a TA Instruments dynamic mechanical analyzer (Model Q800) according to the ASTM D4065-01 standard under a dual cantilever beam mode. The temperature was ramped from 30 °C to 200 °C at a rate of 10 °C/min. TMA tests were carried out on a TA instruments thermo mechanical analyzer (Model Q400) operating at a heating rate of 10 °C/min from 30 °C to 200 °C.

3. Results and Discussions

3.1 Flexural properties of nanocomposites

The typical stress-strain behavior of neat and nanophased composites has been shown in Figure 1. Significant non-linearity is observed in stress strain curve. Due to the higher aspect ratio and specific surface area of GNP, they can effectively inhibit crack generation and crack propagation in the matrix and thus contribute in enhancing the stiffness and strength of nanophased composites. The positive reinforcing effect of GNP addition is evident from Figure 1. From Figure 1, it can be observed that both flexural modulus and strength were enhanced by 40% and 20% in the 0.4 wt% GNP-loaded sample compared to those of the conventional one. As GNPs are layered structures, proper exfoliation and uniform dispersion of GNP in resin are very important to enhance the properties of nanocomposites, which can be attained by the combination of sonication and three roll mixer.

The amine functional groups of GNP and the epoxide groups of DGEBA resin, which consists of ring opening reactions followed by a cross-linking reaction. This crosslink reaction creates an interlocking structure in the resin blend through the covalent bond, which results in impediment in the mobility of polymer chains in the system. Interfacial interaction may have facilitated stress transfer during loading and thus resulted in an increase in flexural properties up to 0.4 wt% loading. However, a slight drop in flexural strength and flexural modulus were observed for 0.5 wt% loading of the GNP. This drop in flexure strength and modulus might be attributed to the formation of excessive agglomeration. These agglomerates can act as stress risers and also increase the free volume by creating voids in the matrix [26].
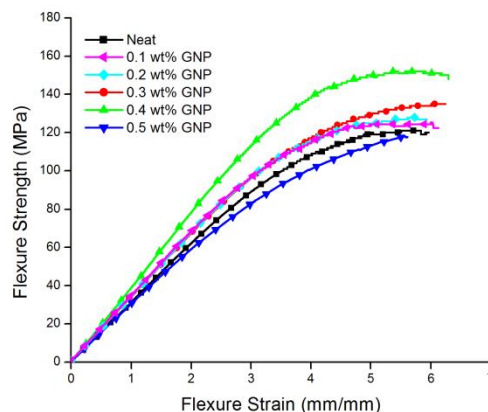

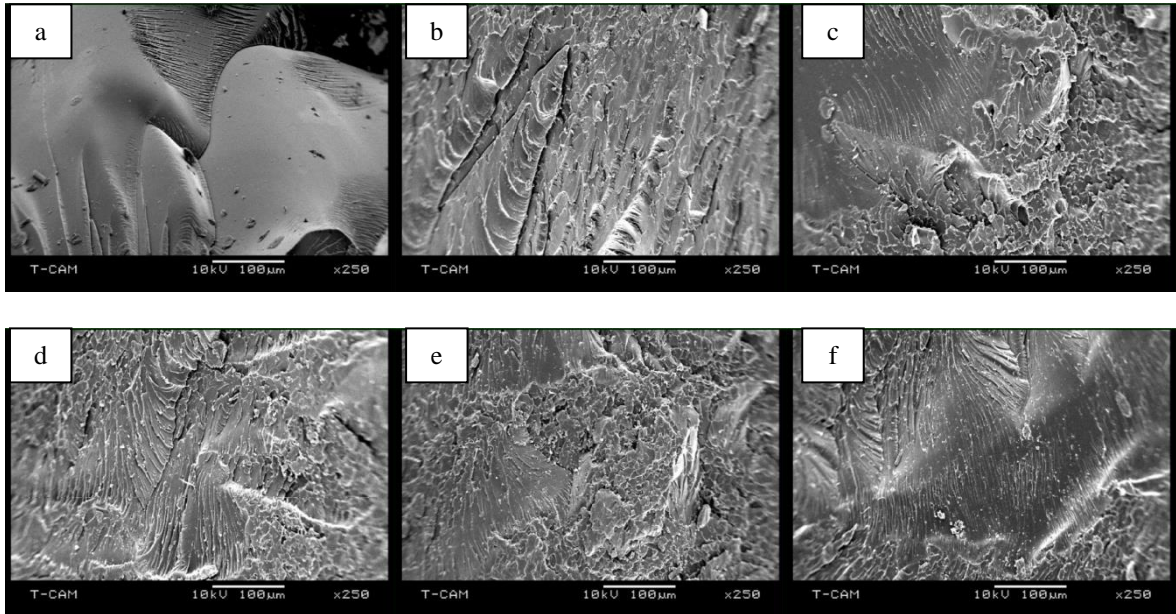Figure 1. Flexural Stress vs. strain response of control and GNP reinfroced epoxy samples

Figure 2. SEM images of fracture surface of (a) neat, (b) 0.1wt%, c) 0.2 wt%, d) 0.3 wt%, e) 0.4 wt%, and f) 0.5 wt% GNP/epoxy composites.

Figure 2 shows the SEM micrographs of neat and nanophased composites fractured surfaces obtained from the three point bending test. Neat epoxy's fracture surface was notably smooth. In Figure 2 (a), it can be observed that the resin crack generated away from any interruption. When epoxy resin was reinforced with nanoparticles, infused nanoparticles obstructed the propagation of cracks in nanocomposites. Moreover, nanoparticles pullout occurred during the crack propagation. In Figure 2 (b)-(f) from the SEM micrographs of fractured surfaces, it is plainly detected that the nanoparticle pullout left a rough surface.

3.2. Dynamic mechanical analysis (DMA)

Figure 3 (a) shows the temperature dependence of storage modulus where temperature is in the range of 30-200 °C. Viscoelastic properties increase significantly with the addition of GNP concentration up to the 0.4 wt%. Storage modulus was improved gradually with the addition of the GNP and the maximum improvement of 16% was observed in the 0.4 wt% loaded GNP sample at 30 °C. Enhanced interaction between well dispersed nanofillers and the matrix has aided this improvement. More sites for GNP/polymer interaction might have been provided by better strong possibility to abridge the epoxy chain molecular motion around GNPs. This abridgement may have resulted in a significant change of elastic and viscous properties in nanocomposites. Figure 3(b) illustrates the variation of T_g with respect to the GNP loading. Maximum is seen to be observed in the 0.4 wt% sample.
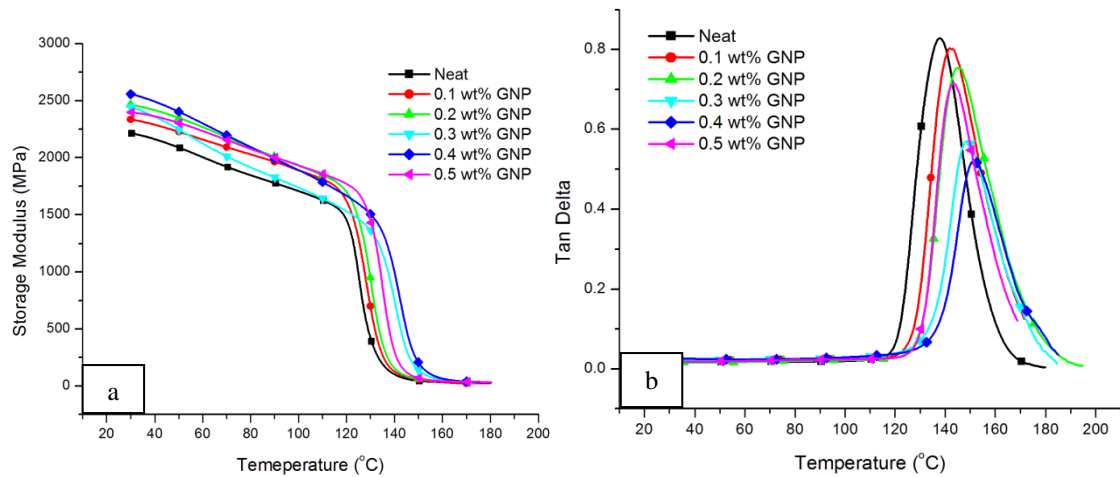
Figure 3. a) Storage modulus b) Tan Delta plot of control and GNP reinforced epoxy nanocomposites.

Glass transition temperature (T_g) for 0.4 wt% GNP reinforced composites increases 10% compared to control samples. The rise in T_g in the polymeric system is predominantly affected by the amount and dispersion of GNP, degree of crosslinking, and interfacial interaction [27-28].

3.3 Thermo-mechanical analysis of nanocomposites

For most engineering applications of polymeric composites, coefficient of thermal expansion (CTE) is considered as a very important thermo-mechanical property. Most of the polymeric materials have high CTE value which limits their applications. In order to ensure good dimensional stability, a lower CTE value is expected. GNPs have very low CTE [27]. Hence, it is very well expected that their presence will seriously influence the CTE of the composite material. Figure 4 (a) indicates the change of dimension vs. temperature plot for nanocomposites. Figure 4 (b) compares the CTE values of the control, 0.1, 0.2 0.3, 0.4 and 0.5 wt% GNP reinforced nanocomposites in the temperature range of 30-100 °C, well below the glass transition temperature and after the glass transition temperature as well. The average coefficient of thermal expansion of epoxy composite was measured as 73.27 ppm/°C. The addition of GNP reduced this value and the CTE value for 0.4 wt% GNP infused CFEC was 37% less than the sample without GNP. This improvement was possible because of the good dispersability of GNP into the resin system. As a result, the interfacial characteristics between the epoxy and the GNP got better. Thus, the CTE value is reduced eventually in the GNP infused samples. Since GNPs have almost zero CTE, the addition of GNP with polymer chain may end up with an overall reduction in the CTE of the composite [29].
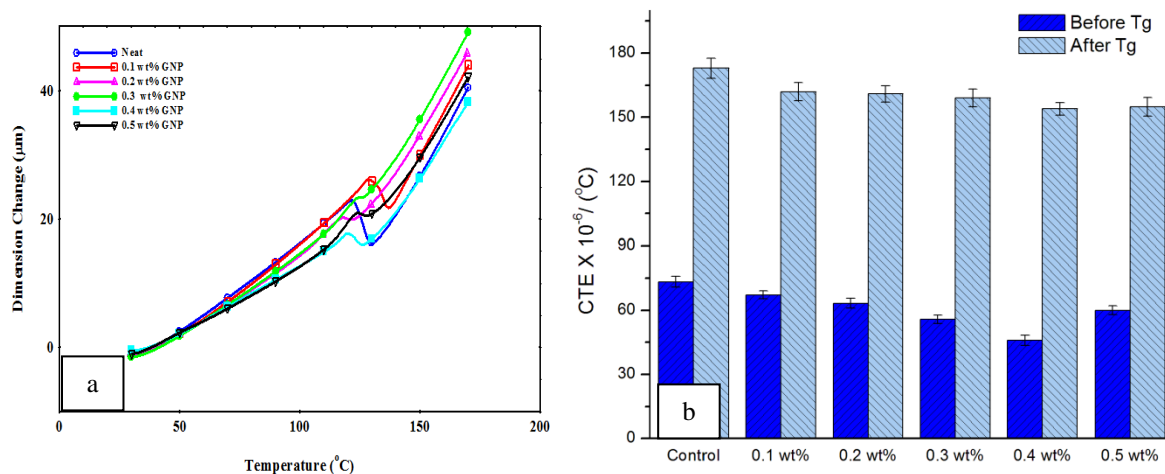
Figure 4. a) Dimension change vs. temperature plot, b) CTE before and after T_g for epoxy nanocomposites

4. Conclusions

Nanoparticles reinforcement enhances almost all the properties of CFRP composites evaluated from tests conducted. 0.4 wt% GNP reinforced CFRP composite exhibited best properties among the nanoparticles reinforced composites. Flexural strength and modulus increased significantly due to GNP incorporation with the highest enhancement of 20% and 40% respectively, for the 0.4 wt% GNP reinforced nanocomposites. The storage modulus was increased by about 15% at the 0.4 wt% GNP-loaded sample compared to the neat epoxy. The glass transition temperature and loss modulus had also been improved with the addition of GNP. Coefficient of thermal expansion was found decreasing with the increase of GNP concentration up to the 0.4 wt% and maximum reduction about 37% was observed for in the 0.4 wt% GNP-loaded sample before the glass transition temperature.

References

[1]   Y. Geng, M. Y. Liu, J. Li, X. M. Shi, and J. K. Kim, Effects of surfactant treatment on mechanical and electrical properties of CNT/epoxy nanocomposites, Compos. Part A Appl. Sci. Manuf. 39 (2008) 1876–1883.
[2]   Z. Spitalsky, D. Tasis, K. Papagelis, and C. Galiotis, Carbon nanotube-polymer composites: Chemistry, processing, mechanical and electrical properties, Progress in Polymer Science, 35 (2010) 357–401.

[3]   C.-E. Hong, J.-H. Lee, P. Kalappa, and S. G. Advani, Effects of oxidative conditions on properties of multi-walled
       carbon nanotubes in polymer nanocomposites, Compos. Sci. Technol., 67 (20017) 1027–1034.
[4]   N. Liu, F. Luo, H. Wu, Y. Liu, C. Zhang, and J. Chen, One-step ionic-liquid-assisted electrochemical synthesis of ionic-
       liquid-functionalized graphene sheets directly from graphite, Adv. Funct. Mater.18 (2008) 1518–1525.
[5]   L. Wang, J. Hong, and G. Chen, Comparison study of graphite nanosheets and carbon black as fillers for high density
       polyethylene, Polym. Eng. Sci., 50 (2010) 2176–2181.
[6]   K. Kalaitzidou, H. Fukushima, and L. T. Drzal, A new compounding method for exfoliated graphite-polypropylene
       nanocomposites with enhanced flexural properties and lower percolation threshold, Compos. Sci. Technol. 67 (2007)
       2045–2051.
[7]   S. Park and R. S. Ruoff, Chemical methods for the production of graphenes, Nat. Nanotechnol. 4, (2009) 217–224.
[8]   S. Stankovich, D. A. Dikin, G. H. B. Dommett, K. M. Kohlhaas, E. J. Zimney, E. A. Stach, R. D. Piner, S. T. Nguyen,
       and R. S. Ruoff, Graphene-based composite materials, Nature, 442 (2006) 282–286.
[9]   T. Ramanathan, A. A. Abdala, S. Stankovich, D. A. Dikin, M. Herrera-Alonso, R. D. Piner, D. H. Adamson, H. C.
       Schniepp, X. Chen, R. S. Ruoff, S. T. Nguyen, I. A. Aksay, R. K. Prud'Homme, and L. C. Brinson, Functionalized
       graphene sheets for polymer nanocomposites, Nat. Nanotechnol., 3 (2008) 327–331.
[10]   G. Eda and M. Chhowalla, "Graphene-based composite thin films for electronics, Nano Lett., 9 (2009) 814–818.
[11]   Y. Liang, Jiajie ; Xu, Yanfei; Huang, Yi;Zhang, Long; Wang, Yan; Ma, Yanfeng; Li, Feifei; Guo; Tianying; Chen,
       Infrared-Triggered Actuators from Graphene-Based Nanocomposites, J. Phys. Chem. C, 113 (2009) 9921–9927.
[12]   J. Liang, Y. Huang, L. Zhang, Y. Wang, Y. Ma, T. Cuo, and Y. Chen, Molecular-level dispersion of graphene into
       poly(vinyl alcohol) and effective reinforcement of their nanocomposites, Adv. Funct. Mater. 19 (2009) 2297–2302.
[13]   C. Lee, X. Wei, J. W. Kysar, and J. Hone, Measurement of the elastic properties and intrinsic strength of monolayer
       graphene, Science, 321 (2008) 385–388.
[14]   L. G. Van, A. C. Van, D. V Van, and P. Geerlings, Ab initio study of the elastic properties of single-walled carbon
       nanotubes and graphene, Chem. Phys. Lett., 326 (2000) 181–185.
[15]   M. A. Rafiee, J. Rafiee, Z. Wang, H. Song, Z. Z. Yu, and N. Koratkar, Enhanced mechanical properties of
       nanocomposites at low graphene content, ACS Nano, 3 (2009) 3884–3890.
[16]   A. Yasmin and I. M. Daniel, Mechanical and thermal properties of graphite platelet/epoxy composites, Polymer 45
       (2004) 8211–8219.
[17]   A. Yasmin, J. J. Luo, and I. M. Daniel, Processing of expanded graphite reinforced polymer nanocomposites, Compos.
       Sci. Technol., 66, (2006) 1179–1186.
[18]   S. Chandrasekaran, C. Seidel, and K. Schulte, Preparation and characterization of graphite nano-platelet (GNP)/epoxy
       nano-composite: Mechanical, electrical and thermal properties, Eur. Polym. J.. 49 (2013) 3878–3888.
[19]   M. Fang, Z. Zhang, J. Li, H. Zhang, H. Lu, and Y. Yang, Constructing hierarchically structured interphases for strong
       and tough epoxy nanocomposites by amine-rich graphene surfaces, Journal of Materials Chemistry 20 (2010) 9635.
[20]   X. Wang, W. Xing, P. Zhang, L. Song, H. Yang, and Y. Hu, Covalent functionalization of graphene with organosilane
       and its use as a reinforcement in epoxy composites, Compos. Sci. Technol. 72 (2012) 737–743.
[21]   P. C. Ma, S. Y. Mo, B. Z. Tang, and J. K. Kim, Dispersion, interfacial interaction and re-agglomeration of
       functionalized carbon nanotubes in epoxy composites, Carbon 48 (2010) 1824–1834.
[22]   J. Shen, W. Huang, L. Wu, Y. Hu, and M. Ye, The reinforcement role of different amino-functionalized multi-walled
       carbon nanotubes in epoxy nanocomposites, Compos. Sci. Technol. 67 (2007) 3041–3050.
[23]   F. Gojny, M. Wichmann, B. Fielder, and K. Schutle, Influence of different carbon nanotubes on the mechanical
       properties of epoxy matrix composites – A comparative study, Compos. Sci. Technol. 65 (2005) 2300–2313.
[24]   S. Wang, P. J. Chia, L. L. Chua, L. H. Zhao, R. Q. Png, S. Sivaramakrishnan, M. Zhou, R. G. S. Goh, R. H. Friend, A.
       T. S. Wee, and P. K. H. Ho, Band-like transport in surface-functionalized highly solution-processable graphene
       nanosheets, Adv. Mater. 20 (2008) 3440–3446.
[25]   G. Wang, X. Shen, B. Wang, J. Yao, and J. Park, Synthesis and characterisation of hydrophilic and organophilic
       graphene nanosheets, Carbon 47, (2009) 1359–1364.
[26]   J. Zhang, AY; Li, DH; Zhang, DX; Lu, HB; Xiao, HY; Jia, Qualitative separation of the effect of voids on the static
       mechanical properties of hygrothermally conditioned carbon/epoxy composites, Express Polym. Lett. 5 (2011) 708–716.
[27]   S. Ganguli, A. K. Roy, and D. P. Anderson, Improved thermal conductivity for chemically functionalized exfoliated
       graphite/epoxy composites, Carbon 46 (2008) 806–817.
[28]   M. Abdalla, D. Dean, D. Adibempe, E. Nyairo, P. Robinson, and G. Thompson, The effect of interfacial chemistry on
       molecular mobility and morphology of multiwalled carbon nanotubes epoxy nanocomposite, Polymer 48 (2007) 5662–
       5670.
[29]   A. Godara, L. Mezzo, F. Luizi, A. Warrier, S. V. Lomov, A. W. van Vuure, L. Gorbatikh, P. Moldenaers, and I.
       Verpoest, Influence of carbon nanotube reinforcement on the processing and the mechanical behaviour of carbon
       fiber/epoxy composites, Carbon 47 (2009) 2914–2923.

6th BSME International Conference on Thermal Engineering (ICTE 2014)

Physical, Mechanical and Thermal Properties of Jute and Bamboo Fiber Reinforced Unidirectional Epoxy Composites

Subhankar Biswas[a,b], Sweety Shahinur[a,c*], Mahbub Hasan[a] and Qumrul Ahsan[a,d]

[a]Department of Materials and Metallurgical Engineering, Bangladesh University of Engineering and Technology, Dhaka 1000, Bangladesh

[b]Department of Mechanical Engineering, Faculty of Engineering and Built Environment, The University of Newcastle, University Drive, Callaghan, NSW 2308, Australia

[c]Bangladesh Jute Research Institute, Mania Mia Avenue, Dhaka, Bangladesh

[d]Department of Engineering Materials, Faculty of Manufacturing Engineering, Universiti Teknikal Malaysia, Hang Tuah Jaya, 76100 Durian Tunggal, Melaka, Malaysia

Abstract

A detailed investigation of physical, mechanical and thermal properties of jute and bamboo fiber reinforced epoxy resin unidirectional void free composites was carried out. The composites were prepared by using vacuum technique. Scanning electron microscopic analysis, tensile and flexural testing and thermogravimetric analysis were performed in order to evaluate surface morphology, mechanical properties and thermal behavior of the unidirectional composites respectively. The relationship between theoretical and experimental values was figured out using rules of mixture. The analytical results showed good agreement with the experimental results. Comparing jute and bamboo fiber reinforced unidirectional composites, it is observed that bamboo fiber reinforced epoxy composites showed good results in terms of tensile strength, while jute fiber reinforced epoxy composites had higher Young's modulus values. Bamboo fiber reinforced epoxy composites showed good flexure strength in the longitudinal distribution. On the other hand, jute fiber reinforced epoxy composited had better flexural strength with transverse fiber distribution in the composites. Fiber distribution was not uniform for both bamboo and jute fiber reinforced unidirectional epoxy composites. Scanning electron microscopic analysis showed that morphological changes took place depending on the fiber orientation in epoxy composites. It is also observed from thermogravimetric analysis that jute fiber reinforced epoxy composites had better thermal behavior compared to bamboo fiber reinforced epoxy composites.

_____

* Corresponding author. Tel.: +8801710894583
  E-mail address: sweetybjri@yahoo.com

1. Introduction

Natural fiber reinforced composites (NFRC) are finding much interest as a substitute for glass or carbon reinforced polymer composites recently. Some advantages associated with using natural fibres as reinforcement in polymers are their non-abrasive nature and low energy consumption. Natural fibres sequester CO_2 from the atmosphere, hence provide an advantageous contribution to the global carbon budget. The easy disposal of natural fiber composites is also important, since they can be easily combusted or composted at the end of their product life cycle. Next to the cost benefits compared to synthetic fibers, natural fibers comparably offer high security if used for automotive applications as an example [1]. Additionally, natural fibres have low density and high specific properties. The specific mechanical properties of natural fibres are comparable to those of traditional reinforcements [2-4]. Thus, the intrinsic properties of natural fibres can satisfy the requests of the global market [5] especially for those industries concerned in weight reduction [6]. That is why they can be potential substitute for non-renewable synthetic fibres [7]. However, high moisture absorption, poor wettability and insufficient adhesion between untreated fiber and polymer matrix lead to debonding at fibre-matrix interface [8]. Again, biodegradable fibres need to be reinforced to improve their properties [9-11]. In present study, epoxy, the most common thermoset resin material was used as a polymer for jute and bamboo fibers. The objectives of this study are to determine the physical, mechanical and thermal properties of unidirectional jute and bamboo fiber reinforced epoxy composites.

2. Experimental

Jute fibers (*corchorus olitorius*) (diameter between 39 to 66 μm) were extracted by mechanical process and supplied by Bangladesh Jute Research Institute (BJRI), Bangladesh. Bamboo fibers (diameter between 178 to 181 μm) were extracted by steam explosion method and supplied by the Hanoi University of Technology, Vietnam. Epoxy resin (Prime^{TM} 20LV) was provided by Gurit (Kassel) GmbH, Germany. The tensile strength (cured), modulus and densities of the epoxy resin used were 68.6 MPa, 2.97 GPa and 1.15 g/cm^3 respectively. For preparing the composites, a defined stacking sequence (eight layers of aligned jute and six layers of aligned bamboo) of bamboo and coir fiber across the aluminium plate was arranged. Upper side of the aligned fibers were covered by pupe paper. A thick flexi glass sheet was used on the upper side to prevent rough surface of the composite. Finally the aligned fibers were surrounded by polypropylene sheet using tacky tape to make sure that there is no air flow. After that one side of the mould system was added with air vacuum machine and another side was doped in resin bath (mixed with hardener) with using Teflon tube. Void was removed from resin mixture using vacuum desiccator. Liquid resin was pumped into the system through the tube which infiltrated the fibres and consequently filled the mould cavity. The resin supply was suspended when the mould was filled up with resin. Both resin and air vacuum tube was sealed and then processed in a Pinette press (hot press) in order to get desired thickness. Heat was applied (at 65^0 C for 1 hour) for curing the resin. When the resin became completely cured, the composite was removed. Tensile tests of unidirectional composites were subsequently carried out following ASTM D638 using an Instron 3369 machine. The cross-head speed was set at 10 mm/mim. An extensometer was placed at the middle portion of the specimen. Load cell of the machine was 30 kN. Flexural tests of the composites were carried out using ASTM D790-03 standard method. Both transverse and longitudinal fiber oriented composites were tested. All the specimens were dried in a vacuum woven at 60^{0}C during 24 hours and then they were left in the tensile testing room 72 hours before testing to assure good conditioning. The temperature and relative humidity was approximately 30^{0}C and 50% respectively. The crosshead speed was set at 0.85 mm/min and 1 kN loadcell was used during the test. The surface morphology and interfacial bonding between the UD jute and coir fiber with epoxy resin in manufactured

composites were examined using a scanning electron microscope (JSM-6701F, JEOL Company Limited, Japan). Thermogravimetric analysis (TGA) was conducted using SDT Q600 T.A Instrument machine under nitrogen atmosphere for untreated jute and bamboo fibers.

3. Results and Discussion

3.1. Tensile properties

Table 1 shows tensile properties of jute and bamboo fiber reinforced epoxy unidirectional composites. In comparison of jute and bamboo fiber UD composites, bamboo fiber reinforced composites had higher tensile strength and strain to failure. However jute fiber composites had higher Young's modulus as compare to bamboo fiber composites. The rule of mixture was used to calculate the theoretical strength and modulus of jute and bamboo fiber epoxy resin composites. The theoretical tensile strength of the jute and bamboo fiber reinforced epoxy composites was found to be 225 and 451 MPa respectively. The experimental values of tensile strength of those composites were 216 and 392 MPa respectively. Thus the experimental results were a bit smaller compared to the theoretical values. Nevertheless, it is important to note that the fibres were not perfectly aligned as shown in Figure 1. Also in the case of jute fiber composites, some of the fibres were crushed during composite fabrication, which is also observed from the SEM morphology.

Table 1. Tensile properties of UD jute and bamboo fiber reinforced epoxy composites.

Name of the fiber	Tensile strength (MPa) ± STD	Young's modulus (GPa) ± STD	Stain to failure (%) ± STD
Jute (52 wt%)	216 ± 1.02	31 ± 1.34	0.78 ± 0.05
Bamboo (57 wt%)	392 ± 8.51	29 ± 1.25	1.38 ± 0.02

The measured Young's modulus of jute and bamboo fiber reinforced composites were 31 and 29 GPa respectively (Table 1), whereas calculated theoretical values were 29 and 36 GPa for jute and bamboo fiber composites. Theoretical results obtained in previous research were in the range of 13-54 GPa for jute fiber composites [12] and 11-30 GPa for bamboo fiber composites [13, 14]. This discrepancy is most likely due to the difficulty of measuring the displacement during the single fiber tensile test by an external tool and possible slippage in the clamps during the tensile test of single fiber leading to an underestimation of fiber modulus. Comparing the tensile strength of jute and bamboo fiber reinforced composites with other natural fiber reinforced composites [15], it is clearly seen that bamboo fiber composites had much higher values. When the density is taken into account, several natural fibres show performance comparable with synthetic fibres like glass fibres. Since this is the case for bamboo and jute fibers, they look set to compete in terms of specific properties with glass fibres in various applications. SEM images are a practical way of confirming the adhesion between fiber and matrix. Images of fracture surfaces reveal whether the fiber bundles are actually impregnated by the matrix or not. The good interface quality is demonstrated in Figure 2 where the fiber surface with trace of the matrix is observed. These micrographs also show that the fibres were pulled out from the matrix rather than broken for bamboo fiber composites and vice versa for the jute fiber composites. Fibers were debonded before pull out. This reveals that there may be formation of mechanical interlocking or chemical bonding between fiber and matrix. Obviously the shrinkage of the matrix will always impose a compressive load that insists the mechanical interlocking between the fibres and matrix.
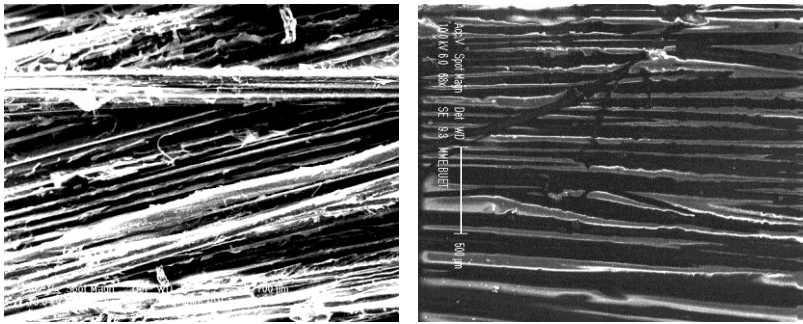
Fig. 1. SEM micrographs of UD fiber reinforced epoxy composites using (a) bamboo and (b) jute.
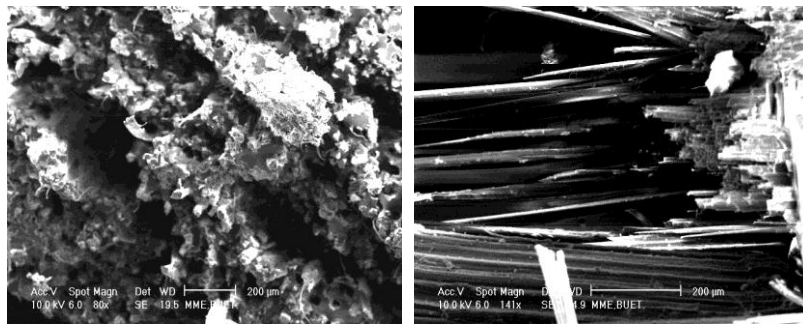

Fig. 2. SEM images of the tensile fracture surface of UD fiber reinforced epoxy composites using (a) jute and (b) bamboo.

3.2. Flexural properties

3.2.1. Flexural properties at longitudinal fiber distribution

Table 2 shows the results of flexural test for unidirectional jute and bamboo fiber reinforced epoxy composites. As shown in Table 2, flexural modulus was almost same for both jute and bamboo fiber reinforced epoxy composites. The flexural strength was higher for bamboo fiber composite as compared to jute fiber reinforced composite. This may be due to difference between the extraction processes of two fibers. As described in section 2, bamboo fibers were extracted by steam explosion method, whereas jute fibers were extracted through mechanical process. Apparently the mechanical extraction process gives fibers with rough surface and little amount of lignin.

Table 2. Flexural properties of unidirectional jute and bamboo fiber composites with longitudinal fiber distribution.

Fiber	Flexural strength (MPa) ± STD	Flexural modulus (GPa) ± STD
Jute (52 wt%)	158 ± 18.90	18 ± 1.92
Bamboo (57 wt%)	226 ± 25.13	19 ± 1.32

The experimental flexural strength was lower compared to theoretical ones in concern of both jute and bamboo fiber composites. However in the case of flexural modulus for both fiber composites, the experimental values were very close to theoretical values. The crack profile SEM images of the flexure specimen of UD jute and bamboo longitudinal fiber reinforced epoxy composites from are shown in Figure 3. It is clearly observed from the micrographs that the fibers were broken in the middle bottom portion of the specimen. Closer looks towards the fracture surface shows that the fracture slide parallel to the load direction for jute fiber composites (Figure 3 (a)), while the slide was perpendicular to the load direction for bamboo fiber reinforced composites (Figure 3 (b)).
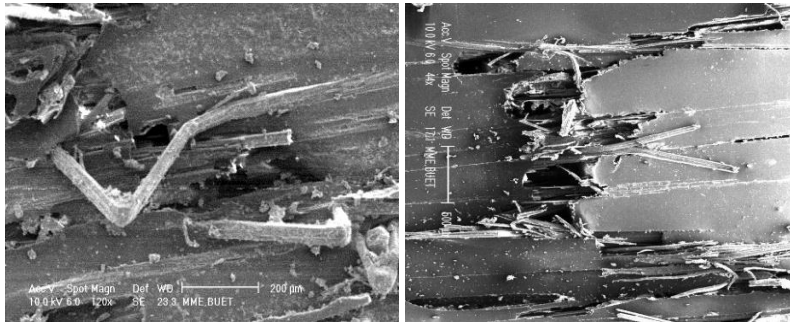
Fig. 3. SEM micrographs of flexural fracture surface of longitudinal fiber reinforced epoxy composites using (a) jute and (b) bamboo.

3.2.2. Flexural properties at transverse fiber distribution

Table 3 shows the flexural properties of unidirectional jute and bamboo fiber reinforced epoxy composites for transverse distribution of fibers. Jute fiber composite was two times higher than that of bamboo fiber composite in terms of transversal flexural strength. Jute fiber composite still had higher modulus value as compared to bamboo fiber composite as jute fiber has more compact structure and broader surface area as compared to bamboo fiber. Compared to natural fiber reinforced thermoplastics, jute and bamboo fiber composites with a thermoset epoxy showed better performance in terms of flexural stiffness. Thermoset resins have low viscosity and require lower processing temperature compared to thermoplastic resins, which clearly benefit the creation of a good fiber/matrix interface. The inclusion in fibers reduced the strength of the epoxy resin. This indicates that the interface was the weakest link in the composite system. Figure 4 shows the SEM micrographs of flexural fracture surface of UD jute and bamboo fiber reinforced epoxy composites in transverse direction. It is observed that fiber could not take any stress as they were aligned to the parallel direction of flexural load.

Table 3. Flexural properties of unidirectional jute and bamboo fiber reinforced epoxy composites for transverse   distribution of fibers.

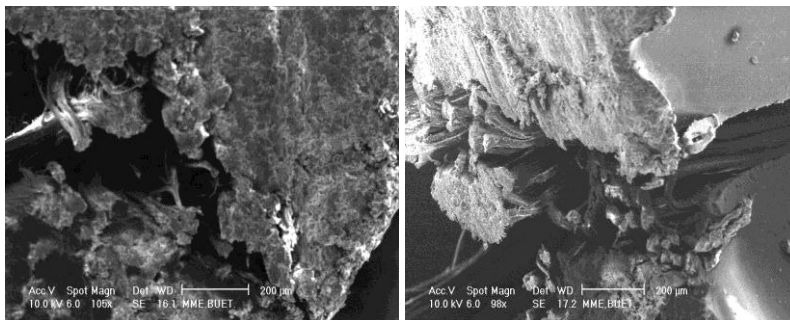| Fiber	Flexural strength (MPa) $\pm$ STD	Flexural modulus (GPa) $\pm$ STD
Jute (52 wt%)	25.7 $\pm$ 2.17	2.73 $\pm$ 0.28
Bamboo (57 wt%)	11.89 $\pm$ 3.87	2.01 $\pm$ 0.11

Fig. 4. SEM micrographs of flexural fracture surface of transverse fiber reinforced epoxy composites with using (a) jute and (b) bamboo.

3.3. Thermogravimetric analysis results

TGA curves for jute and bamboo fiber reinforced epoxy composites are shown in Figures 5 (a) and 5 (b) respectively. There was a peak at approximately 100^0C indicating the removal of moisture for both fiber. Both fibers showed thermal decomposition in the temperature range of 240–260^{0}C. However, the exact thermal decomposition temperature for jute and bamboo fiber epoxy composites was 255^0 and 246^0 respectively. Thus the jute fiber epoxy composite had higher thermal stability as compared to bamboo fiber epoxy composite. During processing of epoxy composites, both jute and bamboo fibers were exposed to high temperature often combined with trapped air, which might cause thermal degradation. If serious degradation of natural fiber occurs at the melt processing temperature, the mechanical reinforcement effect of the fiber is decreased. Thus, TGA analysis was used to determine the high temperature degradation behaviour of the composites under air and nitrogen atmospheres.
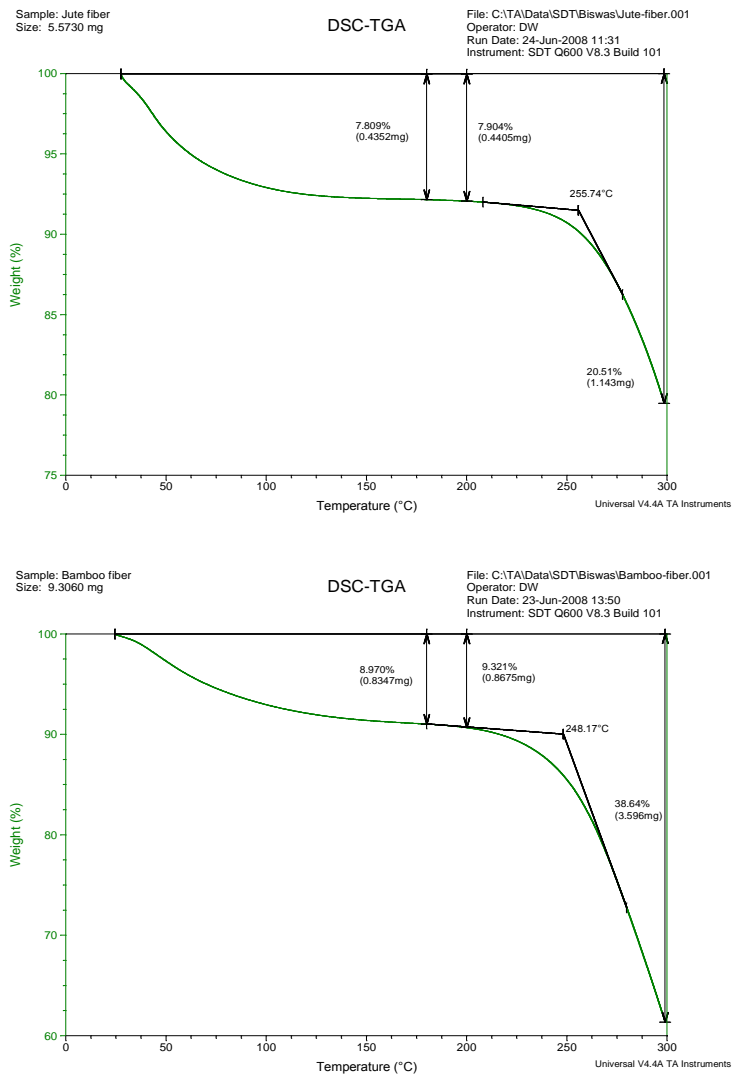

Fig. 5. TGA curves of UD fiber reinforced epoxy composites using (a) jute and (b) bamboo.

4. Conclusions

Void free unidirectional composites were made by using vacuum technique. The analytical results showed good agreement with the experimental results. Bamboo fiber reinforced epoxy had higher tensile strength; while jute fiber reinforced epoxy composites had higher Young's modulus. Bamboo and jute fiber reinforced epoxy composites had better flexure strength with longitudinal and transverse fiber distribution respectively Fibre distribution was not uniformly for both bamboo and jute fiber reinforced UD composites. In case of jute fiber composites, some fiber was broken during processing. It is also revealed that jute fiber reinforced epoxy composites showed better thermal behavior compared to bamboo fiber reinforced epoxy composites.

References

[1] Flemming, M., Ziegmann, G. and Roth, S. (1995). Einfu¨hrung, Faserverbundbauweisen: Fasern und Matrices, pp. 1–5 and 155–179, Springer-Verlag, Berlin, Heidelberg.
[2] Nele Defoirdt, Subhankar Biswas, Linde De Vriese, Le Quan Ngoc Tran, Joris Van Acker, Qumrul Ahsan, Larissa Gorbatikh, Aart Van Vuure, Ignaas Verpoest. Assessment of the tensile properties of coir, bamboo and jute fibre. Composites: Part A 41 (2010) 588–595
[3] S. Biswas, Q. Ahsan, I. Verpoest, and M. Hasan. Effect of Span Length on the Tensile Properties of Natural Fibers. Advanced Materials Research Vols. 264-265 (2011) pp 445-450
[4] Subhankar Biswas, Qumrul Ahsan, Ahmed Cenna, Mahbub Hasan, and Azman Hassan. Physical and Mechanical Properties of Jute, Bamboo and Coir Natural Fiber. Fibers and Polymers 2013, Vol.14, No.10, 1762-1767
[5] A.S. Herrmann, H. Hanselka, H. Nickel, U. Riedel, TECNITEX, Torinto, 1996.
[6] A.K. Mohanty, A. Mubarak, G. Khan, Hinrichsen, Surface modification of jute and its influence on performance of biodegradable jute-fabric, Compos. Sci. Technol. 60 (2000) 1115–1124.
[7] A. Gandini, W. Botaro, E. Zeno, S. Bach, Polym. Int. 50 (2001) 7–9.
[8] Bledzki AK, Gassan J. Einflub von Haftvermittlern auf das feuchterverhalten naturfaserversta¨rkter Kunststoffe. Angew Makromol Chem 1996;236:129–38.
[9] Ma XF, Yu JG, Kennedy JF. Studies on the properties of natural fiberreinforced thermoplastic starch composites. Carbohydr Polym 2005;62:19–24.
[10] Soykeabkaew N, Supaphol P, Rujiravanit R. Preparation and characterization of jute-and flax-reinforced starch-based composite foams. Carbohydr Polym 2004;58(1):53–63.
[11] Tserki V, Matzinos P, Zafeiropoulos NE, Panayiotou C. Development of biodegradable composites with treated and compatibilized lignocellulosic fibers. J Appl Polym Sci 2006;100(6):4703–10.
[12] Munder F, Hempel H. Mechanical and thermal properties of bast fibers compared with tropical fibers. Mol Cryst Liq Cryst 2006;448:197-209.
[13] John MJ, Anandjiwala RD. Recent developments in chemical modification and characterization of natural fiber-reinforced composites. Polym Composite 2008;29(2):188-207.
[14] Ahmed KS, Vijayaraangan S, Naidu ACB. Elastic properties, notched strength and fracture criteria in untreated woven jute-glass fabric reinforced polyester hybrid composites. Mater Design 2007;28(8):2287-2294.
[15] A. K. Mohanty, M. Misra and L. T. Drzal. Surface modifications of natural fibers and performance of the resulting biocomposites: An overview. Composite Interfaces, Vol. 8, No. 5, pp. 313–343 (2001).

6th BSME International Conference on Thermal Engineering (ICTE 2014)

Temperature Dependent Mechanical Behavior of a Locally Restrained Graphite-Aluminum Laminated Plate under Bi-axial Loading

Partha Modak, S. Reaz Ahmed[*]

Department of Mechanical Engineering, Bangladesh University of Engineering and Technology, Dhaka 1000, Bangladesh

Abstract

Temperature-dependent mechanical behavior of a locally restrained metal-matrix composite plate is investigated under uniform bi-axial compression. Thin rectangular plates of angle-ply and cross-ply laminate composed of Graphite-Aluminum composite are considered for the analysis. The plates are assumed to be locally restrained at their corner regions. Temperature-dependent mechanical properties of the metal-matrix composite are used in the displacement-potential analysis of the elastic response. Results of deformed shapes as well as stress distributions are demonstrated as a function of temperature and fiber-orientation of the laminate. © 2015 The Authors. Published by Elsevier Ltd.
Peer-review under responsibility of organizing committee of the 6th BSME International Conference on Thermal Engineering (ICTE 2014).

Keywords: Mechanical behavior; Gr-Al laminate; bi-axial loading; temperature; fiber orientation; displacement potential

1. Introduction

Metal matrix composites are good candidates for aerospace applications that require a wide operating temperature range, high inter-laminar strength, and good impact resistance and lightening tolerance. While significant effort is being devoted to material development and processing, practical application of composite materials lags behind due to the lack of specific design guidance and an understanding of the material performance under actual service conditions.

Graphite fiber-reinforced aluminum composite has attracted interest of materials manufacturers and researchers [1]. Because of low thermal expansion properties and high specific stiffness, graphite-aluminum composites are leading candidates for applications in high precision space vehicles where dimensional stability in a wide temperature range is a major design criterion. The mechanical behavior of graphite fiber composites can be influenced by externally applied parameters, such as, loading, restraints, strain rate, temperature and humidity as well as fiber orientation. Recently, results of studies dealing with the characterization of graphite-aluminum composites under thermo-mechanical loading have been reported [1]. J.M. Lifshitz [2] investigated on mechanical behaviour of a graphite fiber composite under the influence of strain rate, temperature and humidity. A theoretical and experimental study of Al alloy 6061-SiC metal matrix composite was conducted to identify the operative mechanism for accelerated aging [3]. The effect

---

[*] Corresponding author. Tel.: +880-2-966-5636
E-mail address: reaz207@yahoo.com

of addition of silicon carbide filler in different weight percentages on physical, mechanical, and thermal properties of chopped glass fiber-reinforced epoxy composites has been investigated by [4]. On the other hand, the effect of fiber orientation on the mechanical behavior of structural components has now become a key subject in the field of composite structures [5,6]. A useful investigation of the effect of fiber orientation together with the exposure temperature on the stress field of Gr-Al plates is of great practical importance to define and understand the corresponding mechanical behavior and also for their improved design.

The present paper describes a new investigation of temperature dependent mechanical behavior of a metal matrix laminated plate under uniform bi-axial compression. A 45° angle-ply and a cross-ply laminated composite of P100/6061 Gr-Al are considered for the analysis. The plates are assumed to be locally restrained at their corner regions to simulate the physical condition of tag welding. On-axis mechanical properties of the unidirectional composite obtained at different temperatures are used in the analysis. Displacement potential computational method [7,8] is used to analyze the present mixed boundary value problem of laminated composites. Results of the analysis are presented mainly in the form of deformed shape and stress distributions as a function of temperature and ply angles of the laminates.

2. Theoretical background of the analysis

The stress-strain relations for general laminated composite materials under the plane stress condition are given by [9]

$$\begin{bmatrix} \sigma_{xx} \\ \sigma_{yy} \\ \sigma_{xy} \end{bmatrix} = \frac{1}{h} \begin{bmatrix} A_{11} & A_{12} & A_{16} \\ A_{12} & A_{22} & A_{26} \\ A_{16} & A_{26} & A_{66} \end{bmatrix} \begin{bmatrix} \varepsilon_{xx} \\ \varepsilon_{yy} \\ \varepsilon_{xy} \end{bmatrix} \tag{1}$$

Here, A_{ij} are the elements of extensional stiffness matrix $[A]$ [9], which are various functions of E_1, E_2, G_{12} and v_{12}. h is the total thickness of the laminate. With reference to a rectangular coordinate system (x, y), in absence of body forces, the two differential equations of equilibrium for the problems of symmetric laminated composites, under plane stress approximation, are as follows [9,10]:

$$A_{11}\frac{\partial^2 u_x}{\partial x^2} + 2A_{16}\frac{\partial^2 u_x}{\partial x \partial y} + A_{66}\frac{\partial^2 u_x}{\partial y^2} + A_{16}\frac{\partial^2 u_y}{\partial x^2} + (A_{12} + A_{66})\frac{\partial^2 u_y}{\partial x \partial y} + A_{26}\frac{\partial^2 u_y}{\partial y^2} = 0 \tag{2a}$$

$$A_{16}\frac{\partial^2 u_x}{\partial x^2} + (A_{12} + A_{66})\frac{\partial^2 u_x}{\partial x \partial y} + A_{26}\frac{\partial^2 u_x}{\partial y^2} + A_{66}\frac{\partial^2 u_y}{\partial x^2} + 2A_{26}\frac{\partial^2 u_y}{\partial x \partial y} + A_{22}\frac{\partial^2 u_y}{\partial y^2} = 0 \tag{2b}$$

For a symmetric laminated composite, the mid-plane strains are considered to be the global strains, as the curvature effect under in-plane loading can be neglected [9]. Moreover, for a symmetric laminate with even number of plies, A_{16} and A_{26} are zero. In the displacement-potential lamination theory, a potential function $\psi(x, y)$ is introduced in terms of the displacement components of plane elasticity, as follows:

$$\begin{bmatrix} u_x \\ u_y \end{bmatrix} = \begin{bmatrix} m_1 & m_2 & m_3 \\ n_1 & n_2 & n_3 \end{bmatrix} \begin{bmatrix} \frac{\partial^2 \psi}{\partial x^2} & \frac{\partial^2 \psi}{\partial x \partial y} & \frac{\partial^2 \psi}{\partial y^2} \end{bmatrix}^T \tag{3}$$

Where, m_i and n_i are various material constants. For a symmetric laminated composite, the values of the coefficients are obtained as $m_1 = m_3 = n_2 = 0$, $m_2 = 1$, $n_1 = \frac{-A_{11}}{A_{12}+A_{66}}$ and $n_3 = \frac{-A_{66}}{A_{12}+A_{66}}$. The values of the coefficients are determined in such way that with the definition of $\psi(x, y)$, the first equilibrium equation (2a) is identically satisfied [7]. Therefore, ψ has to satisfy the second equilibrium equation (2b) only. Expressing equation (2b) in terms of the function $\psi(x, y)$, the single governing differential equation of equilibrium for the symmetric laminated composites is obtained as follows:

$$\frac{\partial^4 \psi}{\partial x^4} + \left(\frac{A_{22}}{A_{66}} - \frac{A_{12}^2}{A_{11}A_{66}} - \frac{2A_{12}}{A_{11}} \right) \frac{\partial^4 \psi}{\partial x^2 \partial y^2} + \frac{A_{22}}{A_{11}} \frac{\partial^4 \psi}{\partial y^4} = 0 \tag{4}$$

The explicit expressions of the displacement components in terms of the function are

$$
\begin{bmatrix} u_x \\ u_y \end{bmatrix} = \begin{bmatrix} 0 & 1 & 0 \\ \frac{-A_{11}}{A_{12}+A_{66}} & 0 & \frac{-A_{66}}{A_{12}+A_{66}} \end{bmatrix} \begin{bmatrix} \frac{\partial^2 \psi}{\partial x^2} & \frac{\partial^2 \psi}{\partial x \partial y} & \frac{\partial^2 \psi}{\partial y^2} \end{bmatrix}^T \tag{5}
$$

From equation (1) and (5), the corresponding expressions of stress components in terms of the function, $\psi(x, y)$, are,

$$
\begin{bmatrix} \sigma_{xx} \\ \sigma_{yy} \\ \sigma_{xy} \end{bmatrix} = \frac{1}{h(A_{12}+A_{66})} \begin{bmatrix} 0 & A_{11}A_{66} & 0 & -A_{12}A_{66} \\ 0 & A_{12}^2 + A_{11}A_{66} - A_{11}A_{22} & 0 & -A_{22}A_{66} \\ -A_{11}A_{66} & 0 & A_{12}A_{66} & 0 \end{bmatrix} \begin{bmatrix} \frac{\partial^3 \psi}{\partial x^3} & \frac{\partial^3 \psi}{\partial x^2 \partial y} & \frac{\partial^3 \psi}{\partial x \partial y^2} & \frac{\partial^3 \psi}{\partial y^3} \end{bmatrix}^T \tag{6}
$$

Stresses at individual plies of the laminate are calculated from the global mid-plane strain (ε_{ij}) and the respective transformed reduced stiffness matrix, $\left[\overline{Q}_{ij}\right]$ of the ply [9].

A uniform rectangular mesh-network is used to discretize the plate, which includes an imaginary boundary, immediate exterior neighbor to the physical boundary of the plate. Finite-difference method is used to replace the differential equations associated with the equilibrium and boundary conditions by their corresponding difference equations. The order of local truncation error has been kept the same ($O(h^2)$) for all the expressions developed. Different versions of finite-difference expressions for each of the boundary conditions are developed by adopting various combinations of forward, backward and central difference schemes, for nodal points on different segments of the boundary. Finally, the nodal solutions of the function $\psi(x, y)$ are used to calculate the required displacement, strain and stress fields of the plate through the respective difference equations.

3. Geometry and loading of the laminated plate

The geometry and loading of a locally restrained laminated composite plate subjected to a uniform bi-axial compression is shown in Fig. 1. Two different composite plates of angle-ply and cross-ply laminates are considered for the present analysis. The length, width and thickness of the plate are represented by a, b and h, respectively. Both the plates are composed of eight plies of graphite reinforced aluminum matrix composite of identical thickness, the stacking sequences of which are $[45/-45/45/-45]_s$ and $[0/90/0/90]_s$, respectively. The opposing parallel surfaces of the plate are subjected to uniform compression of identical intensity. The four corner regions of the plate are assumed to be rigidly fixed to simulate the condition of tag welding.
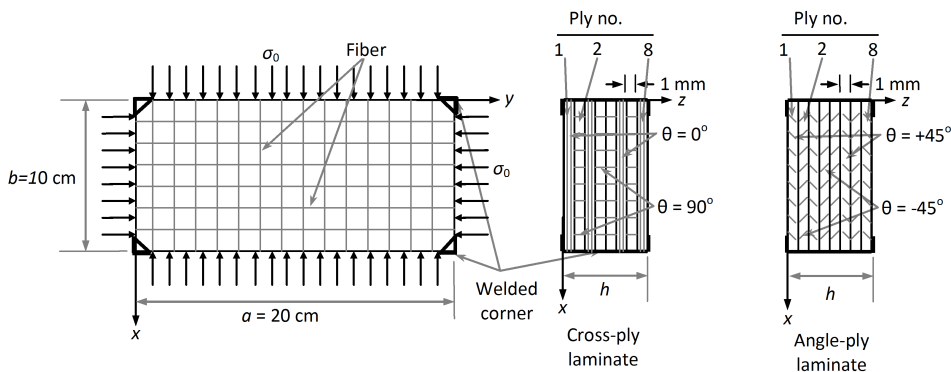

Fig. 1: Geometry, loading and fiber orientation of the laminated plate.

4. Temperature dependent mechanical properties of the composite

The composite material under investigation was composed of Thornel P100 graphite fibers embedded in a 6061 aluminum matrix. It was manufactured by an infiltration/liquid phase hot pressing process. The consolidated panels

were 0.305 by 0.305 m wide and 1.02 mm thick. The average fibre volume fraction of the panels was 46.6%. All mechanical tests were performed on specimens prepared from the above panels. The low thermal expansion coefficient of the graphite fibers in the longitudinal direction along with the high Young's modulus of the P100 fibre make this composite attractive for application requiring a high degree of dimensional stability in a wide temperature range. Tests were performed at four different temperature conditions, which are -101°, 24° (room condition), 121°, and 260^oC [1]. The effective mechanical properties of P100/6061 Gr-Al composite obtained at different working temperatures are listed in Table 1.

Table 1: Mechanical properties of on-axis P100/6061 graphite/Aluminum specimens at different temperatures.

Composite	Property	Symbol	-101^oC	24^oC	121^oC	260^oC
Graphite-Aluminum	Elastic modulus along the fiber direction	E_1 (GPa)	379.9	402.6	392.3	292.9
	Elastic modulus perpendicular to the fiber direction	E_2 (GPa)	29.6	24.1	28.3	24.1
	Shear modulus	G_{12} (GPa)	23.78	19.02	20.89	17.65
	Major Poisson's ratio	v_{12}	0.328	0.291	0.297	0.294

5. Results and discussions

Mechanical behavior of the laminated plates under a uniform bi-axial compression is investigated for four different working temperatures, which are -101°, 24°, 121°, and 260^oC. The plate is kept fixed by local restraints at its four corners, in which the area of each restrained region is only 0.16% of the total plate area. The magnitude of loading intensity is assumed to be $\sigma_0 = 3$ MPa for both the laminates. The thickness of individual plies is kept constant to 1.0 mm. A (53×53) finite-difference mesh-network is used to model the laminated plate of aspect ratio, $a/b = 2$.
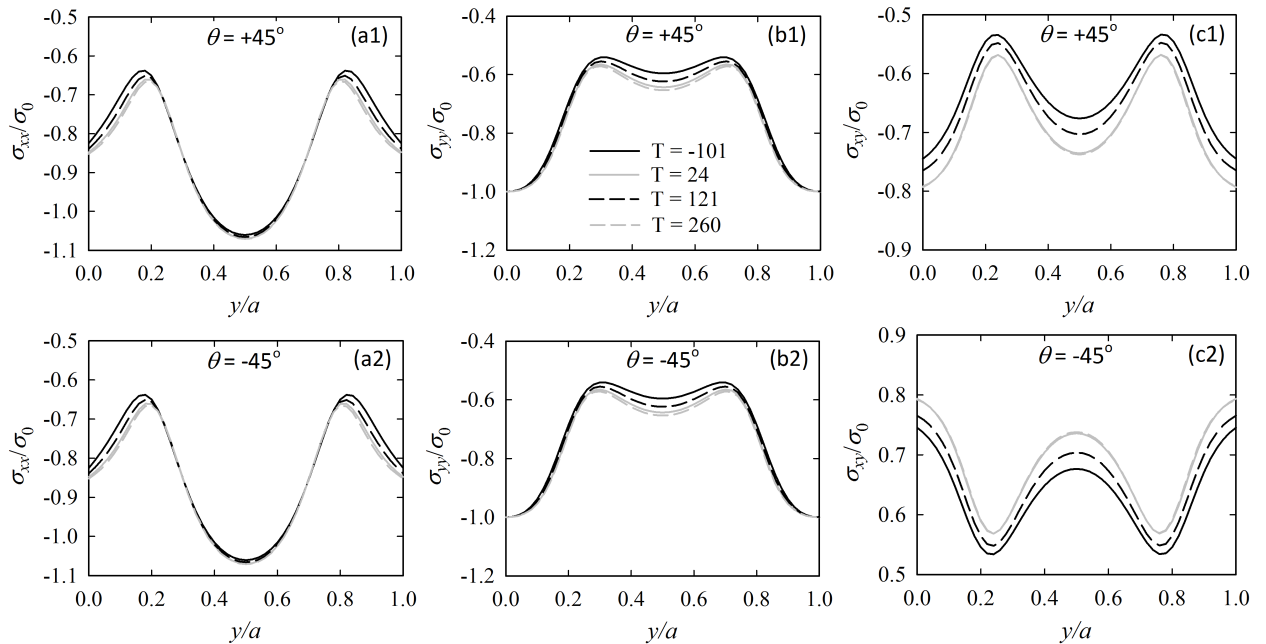

Fig. 2: Distribution of stress components along the mid-section of the angle-ply laminated plate as a function of fiber orientation and temperature.

Figure 2 describes the effect of the variation of temperature as well as fiber orientation of angle-ply laminate on the distribution of the global stresses along the mid-section ($x/b = 0.5$) of the plates. As appears from Fig. 2, both the magnitude and nature of variation of (σ_{xx}/σ_0) are found to be very similar for all the temperature as well as plies of the

angle-ply laminate. A V-shaped distribution of the stresses is encountered, which varies within $0.6 \leq \sigma_{xx}/\sigma_0 \leq 1.1$. For the case of axial stress component, a symmetric M-shaped distribution of stresses is encountered for both the plies. For the case of shear stress, distributions in individual plies are identified to be mirror image of each other, in which the stress level, in general, is found to increase with the increase of temperature. Maximum magnitude of the stress is found at occur at the left and right boundaries of the plate.

Figure 3 shows the distributions of normalized stress components at the the mid-lateral section ($x/b = 0.5$) of the cross-ply laminated plates under bi-axial loading. For the case of lateral stress, both plies assume a flat U-shaped distribution at all temperature levels. Magnitude of stresses is found to be nearly 10 times higher for $\theta = 0^o$–ply compared to that of $\theta = 90^o$–ply. The general trend of distributions for $\theta = 90^o$–ply shows that lateral stress decreases with the increase of exposure temperature. At room temperature condition, the corresponding distribution becomes very close to that at 260^oC, which is however well consistent with the corresponding material properties (Table 1). For the case of axial stress, distributions are found to be different for different plies of the cross-ply laminate, in which stress level is much higher for $\theta = 90^o$–ply compared to that of $\theta = 0^o$–ply. Temperature dependency of stresses is more prominent in cross-ply laminate; in general, with the increase of temperature, stress level decreases for the $\theta = 0^o$–ply, however, an opposite phenomenon is observed for $\theta = 90^o$–ply. Axial stresses are found to assume maximum values at the lateral ends of the plate. On the other hand, the mid-sections of both the plies of the cross-ply laminate are found to be completely free from shearing stresses, which is because of the symmetry of the problem.
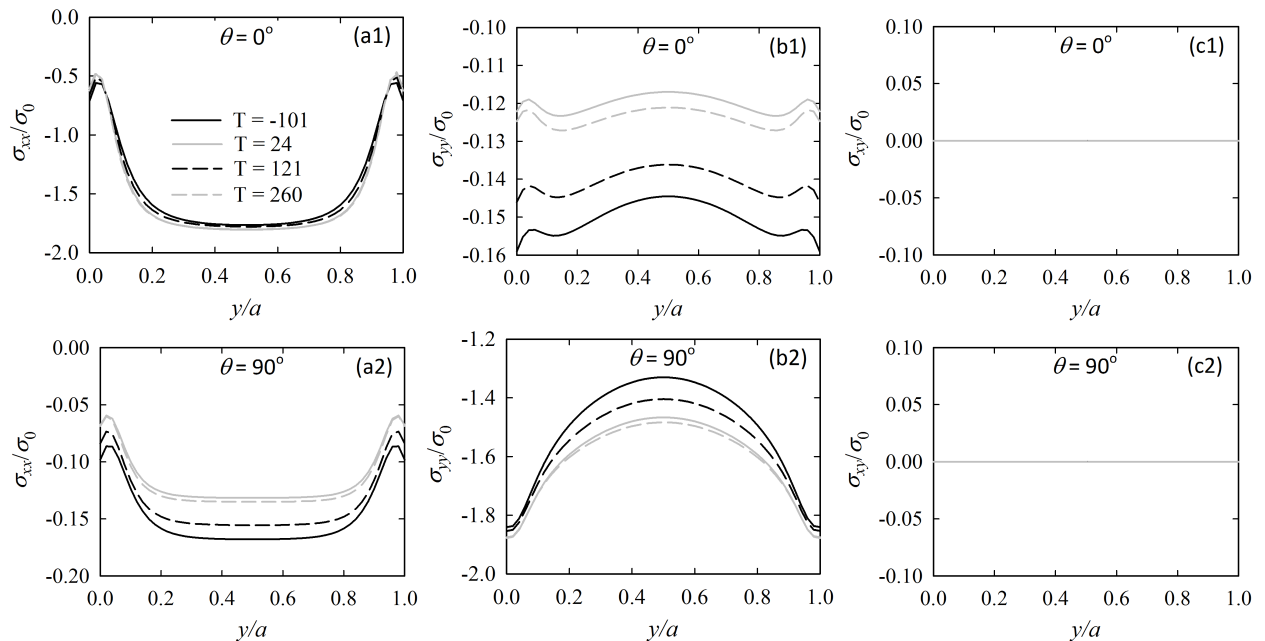

Fig. 3: Distribution of stress components along the mid-section of the cross-ply laminated plate as a function of fiber orientation and temperature.

Figure 4 shows the deformed shapes of the plates obtained at 121^oC together with their un-deformed shapes. The overall deformation pattern of the plate is found to be in good agreement with the physical model of the problem, which verifies the appropriateness of the present modeling. Axial deformation of the angle-ply laminate is slightly higher than that of cross-ply laminate, whereas lateral deformation is, to some extent, higher for the case of cross-ply laminate.

Table 2 lists the critical local stresses developed at the corner restrained regions of the two laminated plates. Local stresses at the restrained sections are found to be higher than the global stresses in both the laminates. Because of the symmetry of the problem, identical stress concentrations are encountered at all the four restrained regions. The cross-ply laminate is identified to be more critical in terms of local stresses.
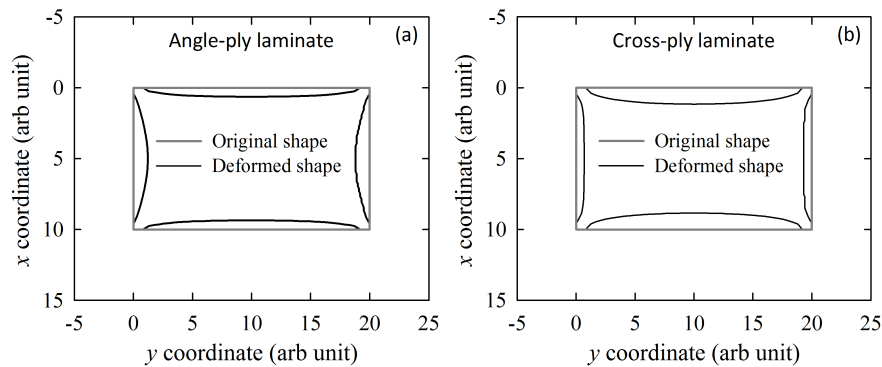
Fig. 4: Deformed shapes of the plate under bi-axial loading (magnification factor, ×1000): (a) Angle-ply, (b) Cross-ply laminate.

Table 2: Local stresses at the restrained corner region of the laminated plates at different temperature.

Section	Normalized stress	Angle-ply laminate				Cross-ply laminate			
		$T = -101^o$	$T = 24^o$	$T = 121^o$	$T = 260^o$	$T = -101^o$	$T = 24^o$	$T = 121^o$	$T = 260^o$
Corner	σ_{xx}/σ_0	1.112	1.017	1.058	0.996	0.674	0.539	0.591	0.511
	σ_{yy}/σ_0	2.279	1.720	1.935	1.614	7.349	7.267	7.297	7.209
	σ_{xy}/σ_0	2.282	2.213	2.248	2.194	2.651	2.373	2.472	2.281

6. Conclusions

Temperature-dependent mechanical behavior of a locally restrained graphite/aluminum laminated plate is investigated under a uniform bi-axial compression. The deformed shapes as well as global stresses are found to be influenced primarily by the ply angle and, to some extent, by the working temperature. The cross-ply laminated plate is identified to be more critical than angle-ply laminate in terms of both local and global stresses. Local stresses are found to be much higher than global ones, which are however highly localized only at the restrained regions.

References

[1] T. Frujita, M.J. Pindera, C.T. Herakovich, Temperature dependent tensile and shear Response of P100/6061 Graphite-Aluminum, in: J.M. Kennedy, H.H. Moller and W.S. Johnson (Eds.), Thermal and Mechanical Behavior of Metal Matrix and Ceramic Matrix Composites, ASTM STP 1080, Philadelphia, 1990, pp. 165–182.

[2] J.M. Lifshitz, Strain rate, temperature and humidity influences on strength, moduli of graphite/epoxy composite, NASA, Ames Research Center, Moffett Field, California, 1981.

[3] I. Dutta, D.L. Bourell, A theoretical and experimental study of Al alloy 6061-SiC metal matrix composite to identify the operative mechanism for accelerated aging, Materials Science and Engineering: A 112 (1989) 67–77

[4] G. Agarwal, A. Patnaik, R. K. Sharma, Thermo-mechanical properties of silicon carbide-filled chopped glass fiber-reinforced epoxy composites, International Journal of Advanced Structural Engineering 5 (2013) 1–8.

[5] D.L. Majid, E.J. Abdullah, N.F. Harun, G.Y. Lim, B.T.H.T. Baharudin, Effect of Fiber Orientation on the Structural Response of a Smart Composite Structure, Procedia Engineering 50 (2012) 445–452

[6] T. Vincent, T. Ozbakkaloglu, Influence of fiber orientation and specimen end condition on axial compressive behavior of FRP-confined concrete, Construction and Building Materials 47 (2013) 814–826

[7] S.R. Ahmed, M.Z. Hossain, M. W. Uddin, A general mathematical formulation for finite-difference solution of mixed-boundary-value problems of anisotropic materials, Computers & Structures 83 (2005) 35–51

[8] S.R. Ahmed, A.A. Mamun, P. Modak, Analysis of stresses in a simply supported composite beam with stiffened lateral ends using displacement-potential field, International Journal of Mechanical Sciences 78 (2014) 140–153

[9] R.M. Jones, Mechanics of Composite Materials, McGraw-Hill, New York, 1975

[10] S. Timoshenko, V.N. Goodier, Theory of Elasticity, third ed., McGraw-Hill, New York, 1979.

6th BSME International Conference on Thermal Engineering (ICTE 2014)

The Effect of Nanoparticles and Alternative Monomer on the Exothermic Temperature of PMMA Bone Cement

Morshed Khandaker* and Zhaotong Meng

University of Central Oklahoma, Edmond, Oklahoma 73034, USA

Abstract

Poly methyl methacrylate (PMMA) cement produce exothermic reaction during its polymerization process, which damage the surrounding bone tissue during orthopedic surgery. Nanoparticles additives (magnesium oxide, hydroxyapatite, chitosan, barium sulfate and silica) and alternative monomers (glycidyl methacrylate(GMA) tri-methaxysilyl propyl methacrylate (3MPMA)), can be incorporated with the PMMA beads and methyl methacrylate (MMA) monomers, respectively, to reduce the exothermic temperature. A comparative study of the addition of these additives and monomer at different concentration on exothermic temperature of PMMA is not known and significant for designing improved PMMA cement for orthopedic applications. The goal of this study is two folds: (1) to evaluate the effect of the inclusion of the above additives with PMMA on the exothermic temperature of PMMA, (2) to evaluate the effect of the inclusion of the above alternative monomers on the exothermic temperature of PMMA. A commercial bone cement was used in this study as PMMA cement. Two wt% and six wt% of the above nanoparticle were mixed with PMMA beads. Two and six wt% of the above alterative monomers were mixed with MMA monomers. Bead and monomer ratio of 2:1 was maintained to prepare the cement samples. A 4-channel thermocouple was used to determine the temperature changes of the samples in an insulated acrylic mold during the curing period. This study found maximum curing temperature on the 2 wt% Magnesium oxide added PMMA specimen was significantly lower than other samples. Addition of 3MPMA and GMA to MMA decreased the maximum curing temperatures and curing time of specimens compared to other samples.

© 2015 The Authors. Published by Elsevier Ltd.
Peer-review under responsibility of organizing committee of the 6th BSME International Conference on Thermal Engineering (ICTE 2014).

Keywords: PMMA; Bone cement; Exothermic Temperature; Additives; Nanoparticles, Orthopedics.

_____

* Corresponding author. Tel.: 1-405-974-5935; fax: 1-405-974-3812.
  E-mail address: mkhandaker@uco.ed

1. Introduction

The most common bone cement material used clinically today for orthopedic surgeries is poly methyl methacrylate (PMMA) [1]. In general, poly Methyl MethAcrylate (PMMA) beads are added to methyl methacrylate (MMA) monomer with bead and monomer ratio of 2:1 to prepare the PMMA bone cement. Conventional PMMA bone cement has several thermal disadvantages. It is known that polymeric materials have an exothermic reaction during its polymerization process [2]. The problem can cause damage to the surrounding bone cells as well as the tissues [3]. Nanoparticle (NP) additives such as magnesium oxide (MgO), hydroxyapatite (HAp), chitosan (CS), barium sulfate ($BaSO_4$) and silica (SiO_2) have been used as additives for the improvement of thermal performances of conventional PMMA bone cement [4]. Glycidyl methacrylate(GMA) and tri-methaxysilyl propyl methacrylate (3MPMA) can be used with MMA to increase the PMMA bone cement thermal properties too. Different types and concentrations of monomers affect the exothermic reaction differently [5]. A comparative study of the effect of the additives and monomers are required for designing improved PMMA cement for orthopedic applications.

It is important to identify if the addition of nanoparticle and alternative monomer with bone cements result in a harmful exothermic process. The exothermic process is a process which the reactants produce heat during the reaction. The process for the PMMA bone cement to solidify is highly exothermic and it can damage the surrounding bone tissue [8]. The more heat it produces during the process, the more harmful it will be to the surrounding bone tissue. Additionally, the residual stresses, caused by the exothermic temperature difference, can influence the fracture energies at the grain boundaries of the nanoparticle-PMMA beads interface [9]. Determining the temperature change of the PMMA cement will provide a good evidence of how much damage the developed cement will cause to the surrounding bone tissue.

The high surface area to volume ratio of nanoparticle additives provides many attractive mechanical, chemical, and thermal qualities regarding bone cement applications. They were previously shown to improve the mechanical performance of acrylic bone cement [10-12]. MgO, HAp, CS, $BaSO_4$ and SiO_2 are attractive as additives in bone cement because they can offer the potential to dissipate the heat generated from polymerization reactions throughout the bone cement material, facilitate more uniform cement curing, and minimize the risk of thermal necrosis.

This research will be a good data resource of exothermic measurement of different monomers in bone cement for further studies to develop novel bone cement. Conducting research on materials will also benefit other branches of engineering, such as strength of materials or structural engineering. Veterans who need amputations will have a better chance to avoid the pain from the dying bone tissues. People who were in accidents or disasters will also have a better chance to have better artificial organs. The aging community will benefit from better biomedical devices to increase the length and quality of life.

2. Materials and Methods

2.1. Sample Preparation

Cobalt™ HV bone cement was used in this study as PMMA cement. Two wt% and six wt% of MgO, HAp, CS, $BaSO_4$ and SiO_2 were mixed with PMMA beads. The mixer was dissolved in MMA monomer using 2:1 solid: liquid ratio to prepare PMMA-MgO, PMMA-HAp, PMMA -CS, PMMA -$BaSO_4$ and PMMA -SiO_2 specimens, respectively. Similarly, two and six wt% of GMA and 3MPMA monomers were mixed with MMA monomers. The solution was dissolved with 2 wt% and 6 wt% of PMMA-MgO, PMMA-HAp, PMMA -CS, PMMA -$BaSO_4$ and PMMA -SiO_2 mixtures using 2:1 solid: liquid ratio to prepare the corresponding GMA and 3MPMA included PMMA-MgO, PMMA-HAp, PMMA -CS, PMMA -$BaSO_4$ and PMMA -SiO_2 specimens.

2.2. Design and manufacture of the experimental setup

A custom made temperature measurement system was used to determine the temperature changes of the different PMMA cements in an insulated acrylic mold. The 4-channel DI-1000 thermocouple (DATAQ Instruments) was used to measure the temperature changes of the bone cements. The thermocouple was connected to a data acquisition device which was connected to a computer. The computer utilized the InstruNet software for collecting the

experimental data. The schematic figure of the setup is shown in the Fig. 1. The experimental setup is shown in the Fig. 2.
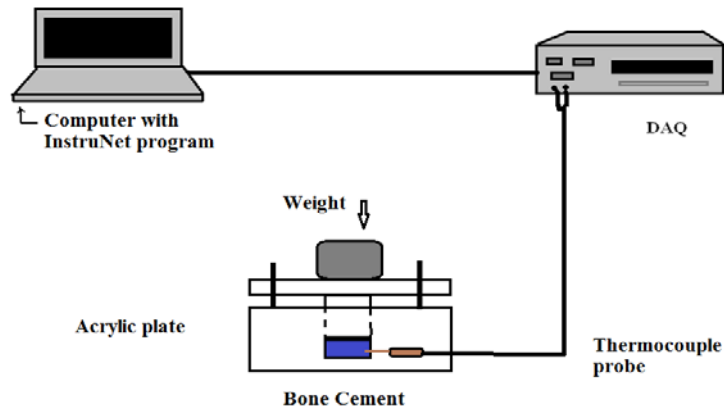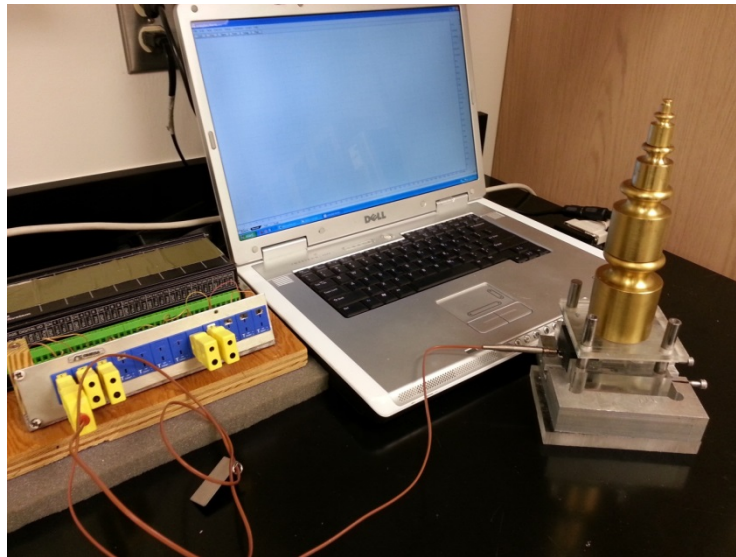

Fig. 1. Schematic diagram for experimental setup

Fig. 2. Fabricated experimental setup.

2.3. Measurement of exothermic temperature

The changes in temperature of PMMA samples during solidification were measured by using a 4-channel DI-1000thermocouple (DATAQ Instruments). The PMMA sample was placed on an acrylic plate. Set of weights (1633 grams) pressing the sample from above. The temperature change was recorded over various periods of time until the PMMA sample was completely solidified (by using a steel needle to poke the sample in order to identify the curing time). The temperature of pure PMMA cement was used as the reference value. For different types of PMMA samples, the temperatures were measured by thermocouple every 25 seconds.

3. Results and Discussion

Figures 3 to 5 show the variation of curing temperature with respect to time for different PMMA samples. All samples showed the similar characteristic of temperature increase to a peak temperature, T_c, and temperature decrease after T_c. It is also evident from the graphs that nanoparticle additives and alternative monomers influenced the time to reach T_c. The time to reach Tc was lowest for PMMA samples without additives and compared to PMMA samples including additives. MgO-included PMMA cement showed the slowest time to reach maximum temperature. Since it is known that thermal stress is proportional to temperature rise, the thermal stress created in PMMA samples must be higher compared to additive-included PMMA samples.
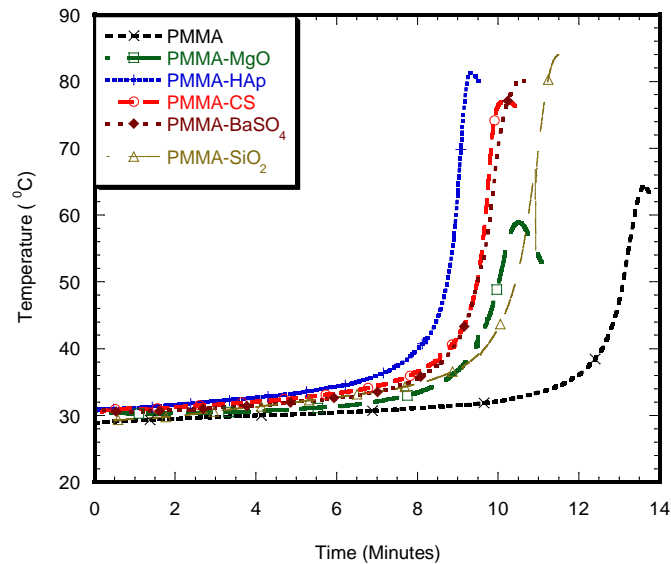

Fig. 3. 2wt% nanoparticle additives with MMA monomer
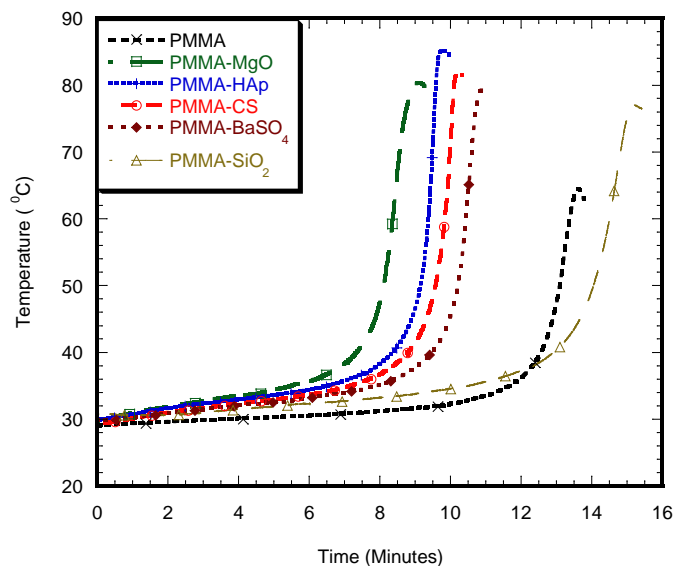

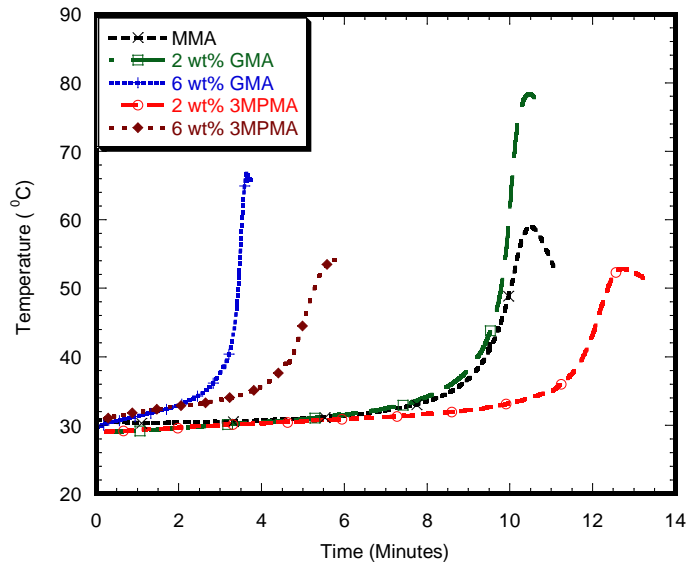Fig. 4. 6wt% nanoparticle additives with MMA monomer
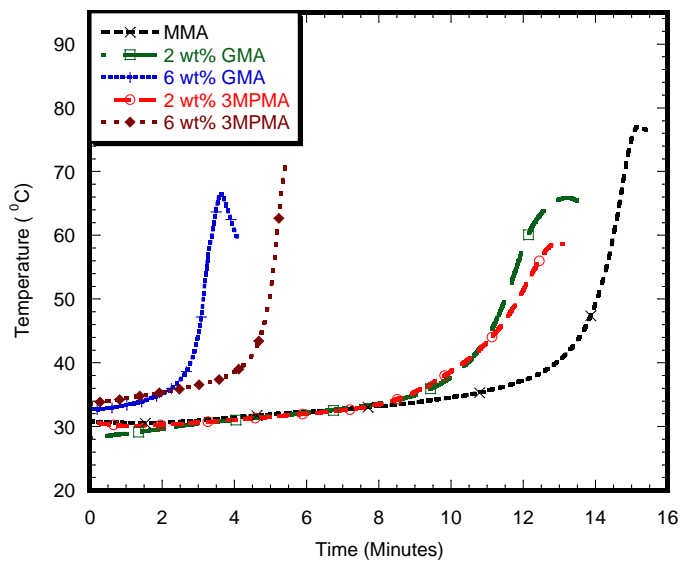
Fig. 5. 2wt% MgO with alternative monomers

Fig. 6. 6wt% SiO2 with alternative monomers

Table 1 and Table 2 report the curing temperatures and times of different samples at different concentrations. This study found that maximum curing temperature on the 2wt% PMMA-MgO with MMA monomer specimen was 58.91 ˚C, which was significantly lower than PMMA specimen as shown in Figure 3. The addition of 2wt%3MPMA to MMA monomer decreased maximum curing temperature for 2wt% MgO as shown in Figure 5. The maximum curing temperature on the 6wt% PMMA-SiO2 with MMA monomer specimen was 77.01 ˚ C, which is significantly lower than other 6wt% specimens, but higher than PMMA specimen as shown in Figure 4. The addition of 2wt%3MPMA to MMA monomer decreased maximum curing temperature for 6wt% SiO2as shown in Figure 6. 2wt% HAp with 2wt% 3MPMA specimen has the lower curing temperature of 49.74 ˚ C by comparing to PMMA-

MMA specimens as shown in Table 1. However, the specimens mixed with higher wt% of GMA monomer had shorter time of curing by comparing to PMMA-MMA specimens as shown in Table 2.

Table 1. Maximum curing temperatures of different specimens

Control (Unit: °C)			NP	MgO		
PMMA	only MMA		Monomer	only MMA	2 wt% GMA	6 wt% GMA
	64.42059		2 wt%	58.9129	78.34302	67.06444
			6 wt%	80.2923	72.35516	70.43481
			Monomer		2 wt% 3MPMA	6 wt% 3MPMA
			2 wt%		52.84161	54.1815
			6 wt%		53.57946	60.6967

NP	Chitosan			BaSO$_4$		
Monomer	only MMA	2 wt% GMA	6 wt% GMA	only MMA	2 wt% GMA	6 wt% GMA
2 wt%	78.08844	81.3611	73.59322	80.2	75.18993	70.51448
6 wt%	82.10461	76.89606	74.64117	79.39277	58.59829	70.75648
Monomer		2 wt% 3MPMA	wt% 3MPM		2 wt% 3MPMA	6 wt% 3MPMA
2 wt%		58.3	69.08008		62.5	75.14077
6 wt%		57	64.3562		54.93084	65.32405

NP	HA			SiO$_2$		
Monomer	only MMA	2 wt% GMA	6 wt% GMA	only MMA	2 wt% GMA	6 wt% GMA
2 wt%	81.32119	77.01936	55.00045	84.12207	83.56549	75.09467
6 wt%	85.15068	57.73536	70.26519	77.00518	65.9138	66.55793
Monomer		2 wt% 3MPMA	wt% 3MPM		2 wt% 3MPMA	6 wt% 3MPMA
2 wt%		49.74053	71.98364		64.03219	73.8733
6 wt%		55.39149	66.80482		58.72564	71.31774

Table 2. Curing times for different specimens

Unit: mins	2wt%GMA					2WT%3MPMA				
	MgO	HA	Chitosan	BaSO$_4$	SiO$_2$	MgO	HA	Chitosan	BaSO$_4$	SiO$_2$
2wt%nanoparticle	7:30	6:44	7:58	7:30	9:37	10:33	11:38	12:10	12:30	11:58
6wt%nanoparticle	8:37	7:50	9:01	8:45	11:07	12:06	12:48	11:30	9:30	11:01
	6wt%GMA					6wt%3MPMA				
	MgO	HA	Chitosan	BaSO$_4$	SiO$_2$	MgO	HA	Chitosan	BaSO$_4$	SiO$_2$
2wt%nanoparticle	7:20	7:22	8:09	7:45	8:50	9:11	8:57	9:33	8:06	9:02
6wt%nanoparticle	7:36	7:21	7:23	6:30	6:45	8:02	9:11	8:33	9:57	9:35
	MMA					PMMA with alternative monomers				
	MgO	HA	Chitosan	BaSO$_4$	SiO$_2$	MMA	2wt%3MPMA	2wt%GMA	6wt%3MPMA	6wt%GMA
2wt%nanoparticle	9:31	7:50	9:10	8:45	10:50	9:55	12:33	10:05	4:55	7:08
6wt%nanoparticle	7:05	7:35	8:15	7:57	10:15					

The results shows that a specific combination of nanoparticle and alternative monomers can significantly and positively affected the thermal properties of Cobalt ^{HV} bone cement. They increased the maximum curing temperature and the time required to completely polymerize the methyl methacrylate monomer, which increases the time required for polymerization. Additional benefits due to nanoparticle and alternative monomer incorporation to bone cement include: minimized risk for thermal necrosis of bone at the bone-cement interfaces that lead to the improved implant longevity in orthopedic and orthodontic applications.

4. Conclusion

The goal for this research was to measure the temperature changes on the different bone cements with different concentrations of nanoparticles (2 wt% and 6 wt% of nanoparticles beads in PMMA beads) and monomers (2 wt% and 6 wt% of alternative monomers in MMA monomers). The maximum curing temperature for 2wt% MgO was significantly lower than the maximum curing temperature for other PMMA specimen having MMA monomer only. However, specimens with higher concentration of nanoparticles had higher maximum curing temperature by comparing to the other PMMA specimen having MMA monomer only. Addition of 3MPMA to monomer decreased the maximum curing temperatures of specimens, but the addition of GMA to monomer decreased the curing time of the specimens.

Acknowledgements

References

[1] J. Van der Geer, J.A.J. Hanraads, R.A. Lupton, The art of writing a scientific article, J. Sci. Commun. 163 (2000) 51–59.
[2] W. Strunk Jr., E.B. White, The Elements of Style, third ed., Macmillan, New York, 1979.
[3] G.R. Mettam, L.B. Adams, How to prepare an electronic version of your article, in: B.S. Jones, R.Z. Smith (Eds.), Introduction to the Electronic Age, E-Publishing Inc., New York, 1999, pp. 281–304.

[1] A. Ricker, P. Liu-Snyder, T.J. Webster, The influence of nano MgO and BaSO4 particle size additives on properties of PMMA bone cement, International Journal of Nanomedicine. (2008) 125–132.
[2] K. Serbetci, F. Korkusuz, N. Hasirci, Thermal and mechanical properties of hydroxypaptite impregnated acrylic bone cements, Polymer Testing. 23-2 (2004) 145-155.
[3] N. J. Dunne, J.F. Orr, Thermal characteristics of curing acrylic bone cement, Journal of Materials Science: Materials in Medicine. 22-2 (2001) 88-97.
[4] M. Khandaker, M. Vaughan, T. Morris, J. White, Z. Meng, Effect of additives particles on mechanical, thermal and cell functions properties of poly (methyl methacrylate) cement, International Journal Nanomedicine. 9-1 (2014) 2699—2712.
[5] B. Pascual, B. Vazquez, M. Gurrachaga, I. Goni , M.P. Ginebra, F.J. Gil, J.A. Planell, B. Levenfield, J. San Roman. New aspects of the effect of size and size distribution on the setting parameters and mechanical properties of acrylic bone cements. Biomaterials. 17-5 (1996) 509-516.
[6] S.B. Kim, Y.J. Kim, T.L. Yoon, S.A. Park, I.H. Cho, E.J. Kim, I.A. Kim, J.-W. Shin, The characteristics of a hydroxyapatite-chitosan-PMMA bone cement, Biomaterials. 25-26 (2004) 5715-5723.
[7] P.C. Liacouras, J.R. Owen, W.A. Jiranek, J.S. Wayne, Effect of pigmentation on the mechanical and polymerization characteristics of bone cement, The Journal of Arthroplasty. 21-4 (2006) 606-611.
[8] V. Alt, T. Bechert, P. Steinrucke, M. Wagener, P. Seidel, E. Dingeldein, E. Domann, R. Schnettler, An in vitro assessment of the antibacterial properties and cytotoxicity of nanoparticulate silver bone cement, Biomaterials. 25-18 (2004) 4383-4391.
[9] S. J. Catharina, H.-C van, L.E. Govaert, A. B. Spoelstra, S.K. Bulstra, G.M.R Wetzels, L.H. Koole, Mechanical behaviour of a new acrylic radiopaque iodine-containing bone cement, Biomaterials. 25-13 (2004) 2657-2667.
[10] Rao M, Su Q, Liu Z, et al. Preparation and characterization of a poly(methyl methacrylate) based composite bone cement containing poly(acrylate-co-silane) modified hydroxyapatite nanoparticles. Journal of Applied Polymer Science. 2014;131(15).
[11] Gutierrez-Mejia A, Herrera-Kao W, Duarte-Aranda S, et al. Synthesis and characterization of core-shell nanoparticles and their influence on the mechanical behavior of acrylic bone cements. Materials Science and Engineering C. 2013;33(3):1737-1743.
[12] Fang C, Hou R, Zhou K, et al. Surface functionalized barium sulfate nanoparticles: Controlled in situ synthesis and application in bone cement. Journal of Materials Chemistry B. 2014;2(9):1264-1274.